Contents lists available at ScienceDirect

Geochimica et Cosmochimica Acta

Magnesium isotope fractionation between calcite and aqueous solutions under elevated temperatures of 98–170 °C

Chuan Liu, Weiqiang Li *

State Key Laboratory for Mineral Deposits Research, School of Earth Sciences and Engineering, Nanjing University, Nanjing, Jiangsu 210093, PR China

ARTICLE INFO

ABSTRACT

The incomplete understanding of Mg isotope fractionation behavior between calcite and aqueous solutions has limited the interpretation and application of Mg isotope data in natural carbonates. In this study, we performed a series of aragonite-to-calcite conversion experiments under hydrothermal conditions to investigate the effects of temperature and organic ligands on elemental and isotopic partitioning of Mg between calcite and aqueous solutions. The experiments produced magnesian calcite via a dissolution-and-precipitation process. The Mg distribution coefficients between solid and aqueous solution (D_{Mg}, 0.08 to 0.21) showed negative correlations with Sr distribution coefficients (D_{Sr}, 0.04 to 0.48), as well as the proportion of calcite in the bulk solid, which indicates mixing of calcite (Mg-rich and Sr-poor) and aragonite (Sr-rich and Mg-poor) in the solid phases. The apparent Mg isotope fractionation factors between solid and aqueous solutions ($\Delta^{26}Mg_{solid-soln}$) show a positive correlation with reaction temperatures, where $\Delta^{26}Mg_{solid-soln}$ increases from ca. $-1.84\,‰$ at 98 °C to $-1.35\,‰$ at 170 °C. In addition, the presence of oxalate contributed to slightly lower $\Delta^{26}Mg_{solid-soln}$ values, which is interpreted to be related to the isotopic effect of Mg-oxalate speciation. Based on the experimental results, we propose a temperature-dependent function for Mg isotope fractionation between calcite and free Mg-aquo ions (i.e., $Mg(H_2O)_6^{2+}$): $\Delta^{26}Mg_{cal-Mg(aq)} = (-0.17 \pm 0.01) \times 10^6/T^2 - (0.52 \pm 0.08)$. This equation is applicable to a wide range of temperatures, especially at hydrothermal conditions, thus enabling interpretations of Mg isotope data from calcite of hydrothermal and burial origin.

© 2022 Published by Elsevier Ltd.

1. Introduction

Magnesium (Mg) is the fourth-most abundant element on Earth and is a major constituent in seawater, as well as various carbonate minerals. Among all the major terrestrial rock types, carbonates exhibit the greatest Mg isotope variability (Teng, 2017 and references therein). Magnesium isotopes in marine carbonate have been used to reconstruct the Mg isotope and chemical compositions of ancient seawater (Higgins and Schrag, 2012; Fantle and Higgins, 2014; Pogge von Strandmann et al., 2014; Li et al., 2015; Gothmann et al., 2017; Crockford et al., 2020), to study the processes of diagenesis (Chanda and Fantle, 2017; Ahm et al., 2018; Fantle et al., 2020; Kimmig et al., 2021), dolomitization (Huang et al., 2015; Ahm et al., 2019; Ning et al., 2020; Hu et al., 2021a), and biomineralization (Chang et al., 2004; Planchon et al., 2013), as well as to constrain geological events such as basin restriction at different scales (Bialik et al., 2018; Hu et al., 2021b).

Understanding the Mg isotope fractionation mechanisms is a prerequisite to applying the carbonate Mg isotope system to trace various geological processes. Numerous experimental studies have been conducted to understand and quantify the Mg isotope fractionation behavior during the formation of different carbonate minerals, including dolomite (Li et al., 2015), magnesite (Pearce et al., 2012), aragonite (Wang et al., 2013), and calcite (Immenhauser et al., 2010; Li et al., 2012; Saulnier et al., 2012; Mavromatis et al., 2013; Chen et al., 2020). In addition, the equilibrium Mg isotope fractionation factors between carbonate mineral and aqueous Mg have been estimated using theoretical calculations (Rustad et al., 2010; Pinilla et al., 2015; Gao et al., 2018; Wang et al., 2019; Son et al., 2020). There are, however, large discrepancies among predictions based on theory and experimental studies, where the magnitude of calculated Mg isotope fractionation factors for calcite (Rustad et al., 2010; Pinilla et al., 2015; Gao et al., 2018; Wang et al., 2019) are generally much greater than those obtained in experimental studies (Immenhauser et al., 2010; Li et al., 2012; Saulnier et al., 2012; Mavromatis et al., 2013; Chen et al., 2020).

* Corresponding author.
  E-mail address: liweiqiang@nju.edu.cn (W. Li).

Inconsistency exists between different experimental studies on Mg isotope fractionation for calcite. Li et al. (2012) reported a $\Delta^{26}Mg_{cal\text{-}soln}$ factor ($\Delta^{26}Mg_{cal\text{-}soln} = \delta^{26}Mg_{calcite} - \delta^{26}Mg_{solution}$) of about -2.5 ‰ at room temperature mainly based on free-drift calcite synthesis experiments, and Chen et al. (2020) reported a similar $\Delta^{26}Mg_{cal\text{-}soln}$ factor of -2.54 ‰ at 298 K based on chemostat calcite synthesis experiments. By contrast, Mavromatis et al. (2013) reported a correlation between precipitation rate and $\Delta^{26}Mg_{cal\text{-}soln}$ for calcite and proposed an equilibrium $\Delta^{26}Mg_{cal\text{-}soln}$ of -3.5 ‰ based on a different type of chemo-stat calcite synthesis experiments. Mavromatis et al. (2017b) further conducted amorphous carbonate (AC) transformation experiments, in which they measured a $\Delta^{26}Mg_{cal\text{-}soln}$ factor of -3.6 ‰ at 298 K upon the transformation of AC to calcite. The discrepancies among these studies have significantly limited the ability to confidently interpret Mg isotopic signatures in natural calcite.

Previous experimental investigations on Mg isotope fractionation for calcite were all conducted at ambient temperatures (Immenhauser et al., 2010; Li et al., 2012; Saulnier et al., 2012; Mavromatis et al., 2013; Chen et al., 2020), where kinetic effects could be introduced due to the high energy barrier associated with dehydration of Mg-aquo ions (Lippmann, 1973; Land, 1998; Immenhauser et al., 2010; Saenger and Wang, 2014). Kinetic isotope effects associated with ion dehydration at low temperatures can be effectively suppressed at elevated temperatures, where relatively high ion-exchange and diffusion rates produce faster attainment of isotopic equilibrium (Li et al., 2015; Shahar et al., 2017). Besides, the low isotope exchange rate would cause a limited degree of isotope exchange between the solid and solution phase, which could introduce considerable uncertainties in extrapolating the equilibrium factors using partial exchange or "three-isotope" techniques (e.g., Cole and Ripley, 1999; Li et al., 2014; Agrinier and Javoy, 2016; Shahar et al., 2017; Trail et al., 2019; Stamm et al., 2022), whereas the increasing reaction temperature could lead to the higher isotope exchange degrees (Saccocia et al., 1998, 2015), thus reducing errors associated with data extrapolation. On the other hand, because stable isotope fractionation factors are temperature-dependent (Bigeleisen and Mayer, 1947; Urey, 1947), Mg isotope fractionation factors obtained at a series of elevated temperatures, where higher rates of isotopic exchange are attained, may be extrapolated to lower temperatures. Such an approach, as had been successfully applied for magnesite and dolomite (Pearce et al., 2012; Li et al., 2015), could reduce or avoid problems of kinetic isotope effects at low temperatures and provide a new solution to the puzzle of Mg isotope fractionation between calcite and aqueous solutions. In this study, we used the hydrothermal conversion of aragonite to Mg-calcite to catalyze isotopic exchange, in the presence of trace organic ligand oxalate, to investigate Mg isotope fractionation between the calcite and aqueous solutions.

2. Experimental methods

The experiments were conducted by reacting aragonite with Mg-containing solutions at hydrothermal conditions (98 to 170 °C), following an experimental concept of mineral conversion previously described by Li et al. (2015). In this study, a small amount of sodium oxalate ($Na_2C_2O_4$) was used in the starting solution, based on a series of exploratory experiments (not shown here; but also see Guo et al., 2019) that demonstrated incomplete conversion of aragonite to calcite on reasonable laboratory time scales (i.e., <100 days) in organic-free Mg-rich aqueous solutions at temperatures below 150 °C. The presence of sodium oxalate in the aqueous solution significantly accelerates conversion of aragonite to calcite even at a low temperature of 98 °C. All experiments

and analyses were conducted at the State Key Laboratory for Mineral Deposits Research, Nanjing University.

2.1. Hydrothermal experiments

Commercially available pieces of coral (*Fungia* sp.) skeletal aragonite from the South China Sea was used as the starting material for the experiments. The coral was leached in 30 % H_2O_2 for 3 days to remove organic matter, then washed with de-ionized water several times and air-dried. The coral was ground to powder with an average particle size of < 60 μm using an agate mortar and pestle prior to experiments. The mineralogy of the powders was confirmed to be pure aragonite by powder X-ray diffraction (XRD) analysis (Appendix Fig. S1). The starting aragonite contains 590 ppm of Mg and 8390 ppm of Sr, corresponding to Mg/Ca and Sr/Ca mole ratios of 2.47 × 10^{-3} and 9.74 × 10^{-3}, respectively (Table 1).

The powders were reacted with either gravimetrically prepared "solution A" (experiment series: 98_A, 110_A, 130_A, 150_A, 170_A), which contained 40 mM $CaCl_2$, 8 mM $MgCl_2$, 0.1 mM $Na_2C_2O_4$, 1.8 mM NaCl, and 0.12 mM $SrCl_2$, or "solution B" (experiment series: 98_B, 130_B, 150_B), which contained 40 mM $CaCl_2$, 8 mM $MgCl_2$, 1 mM $Na_2C_2O_4$ (sodium oxalate) and 0.12 mM $SrCl_2$. The NaCl in solution A compensated the extra Na^+ content induced by higher $Na_2C_2O_4$ in solution B. Hydrothermal conversion experiments were carried out in Teflon-lined stainless steel bombs at 110 °C, 130 °C, 150 °C, and 170 °C, while 15 ml tightly capped PFA beakers were used at 98 °C. For each experiment, 100 mg of aragonite and 10 ml of solution were added to each of the reaction vessels.

The sealed vessels were placed into pre-heated convection ovens at different experiment temperatures. Each set of hydrothermal experiments involved multiple (up to 10) reaction vessels, which were sampled in a time series. Upon removal from the oven and quenched to room temperature in the air within 2 h, the product was transferred to a clean tube, where the solid and fluid contents were separated by centrifuging. The fluid product was centrifuged at 12000 rpm for 1 min three times to remove any possible suspended solids, while the solid product was washed with de-ionized water and centrifuged three times and dried.

2.2. Mineralogical analysis

X-ray diffraction measurements were conducted on a Rigaku Rapid II X-ray diffractometer that was equipped with a rotating Mo K_α source, running at 50 kV and 90 mA. The XRD pattern for the products was collected using a two-dimensional image plate with a 5-minute exposure time. Data treatment and interpretation were performed using a Rigaku 2DP program and Jade 6.5 software. The relative abundance of aragonite and calcite in the solid samples was quantified by the ratio of aragonite (2 2 1) and calcite (1 0 4) reflection intensities (Kontoyannis and Vagenas, 2000). The mineral morphology of the solid samples was characterized on a Hitachi SU1510 variable pressure Scanning Electron Microscope (VP-SEM).

2.3. Solution and solid chemistry analyses

Aliquots of the solid products and solutions were dissolved in 2 % HNO_3 (v/v) to prepare the solutions for elemental analyses. The elemental concentration of the solutions was measured using inductively-coupled plasma optical emission spectroscopy (ICP-OES) with reference to a series of gravimetrically prepared multi-element standard solutions. Specifically, both Mg/Ca and Sr/Ca ratios of solid and solution samples were precisely measured by a combination of the intensity ratio calibration method and sample-standard-sample bracketing method (de Villiers et al.,

Table 1
The mineralogy and chemical composition of solid and solution phases, as well as the fraction of Mg in solution being incorporated into the calcite.

Experimental ID	Temp (°C)	Duration (days)	Mineralogy by XRD	Calcite proportion (%)	pH(25°C)	Ca(mM)	Mg(mM)	Sr(mM)	$(Mg/Ca)_{solid}$ (mM/M)	$(Sr/Ca)_{solid}$ (mM/M)	D_{Mg}	D_{Sr}	Mg incorporation(%)
Starting Aragonite									2.47	9.74			
Starting Solution						39.39	7.87	0.12					
98_A	98	7	Cal + Arg	41.00	7.22	41.00	6.49	0.57	12.22	6.65	0.08	0.48	20.77
	98	14	Cal + Arg	53.95	7.28	40.64	6.30	0.65	17.25	3.87	0.11	0.24	22.36
	98	21	Cal + Arg	58.04	7.24	40.45	6.21	0.70	17.56	3.45	0.11	0.20	23.16
	98	28	Cal + Arg	60.13	7.17	40.61	6.22	0.74	14.59	4.81	0.10	0.27	23.29
	98	35	Cal + Arg	71.40	7.24	40.36	6.09	0.79	18.52	2.33	0.12	0.12	24.40
	98	42	Cal + Arg	83.05	7.20	41.20	6.12	0.79	17.88	2.65	0.12	0.14	25.59
	98	49	Cal + Arg	83.53	7.25	40.52	6.02	0.80	18.81	2.58	0.13	0.13	25.57
110_A	110	5	Cal + Arg	36.90	7.00	41.16	6.51	0.56	13.22	6.17	0.08	0.45	20.78
	110	10	Cal + Arg	61.53	6.89	41.31	6.22	0.71	14.54	4.71	0.10	0.28	24.63
	110	15	Cal + Arg	77.34	7.19	40.10	5.99	0.70	19.72	4.14	0.13	0.24	25.18
	110	20	Cal + Arg	67.12	7.13	40.55	5.88	0.77	22.03	2.50	0.15	0.13	27.39
	110	25	Cal + Arg	81.94	7.08	40.78	5.84	0.81	21.71	2.07	0.15	0.10	28.27
	110	30	Cal + Arg	63.54	7.17	40.86	5.83	0.83	22.77	2.56	0.16	0.13	28.61
	110	35	Cal + Arg	70.75	7.08	40.28	5.78	0.81	22.01	2.32	0.15	0.12	28.18
	110	40	Cal + Arg	90.01	6.95	40.24	5.73	0.87	21.67	2.67	0.15	0.12	28.69
	110	45	Cal + Arg	89.27	7.16	40.47	5.86	0.84	22.41	1.63	0.15	0.08	27.50
	110	50	Cal + Arg	92.97	7.18	40.02	5.98	0.84	22.94	1.68	0.15	0.08	25.19
130_A	130	4	Cal + Arg	40.77	7.10	41.07	6.18	0.62	17.60	4.67	0.12	0.31	24.65
	130	8	Cal + Arg	55.19	7.16	40.75	5.87	0.73	21.52	3.98	0.15	0.22	27.91
	130	12	Cal + Arg	74.57	7.21	40.56	5.85	0.73	21.12	2.89	0.15	0.16	27.82
	130	16	Cal + Arg	87.19	7.02	41.45	5.75	0.83	23.96	2.38	0.17	0.12	30.52
	130	20	Cal + Arg	84.35	7.19	40.56	5.42	0.85	23.43	1.80	0.18	0.09	33.10
	130	24	Cal + Arg	97.24	7.06	41.56	5.48	0.85	25.18	1.56	0.19	0.08	33.95
	130	28	Cal + Arg	88.64	7.15	40.92	5.55	0.78	22.97	1.45	0.17	0.08	32.03
	130	32	Cal + Arg	99.00	7.22	41.08	5.34	0.87	25.40	0.83	0.20	0.04	34.94
	130	36	Cal + Arg	88.74	7.21	40.65	5.64	0.86	24.03	1.61	0.17	0.08	30.48
	130	40	Cal + Arg	99.38	7.13	40.80	5.30	0.83	25.57	1.12	0.20	0.06	34.90
150_A	150	3	Cal + Arg	52.17	6.93	41.04	5.90	0.65	18.81	5.01	0.13	0.32	28.05
	150	6	Cal + Arg	80.80	7.03	41.16	5.72	0.71	21.76	3.38	0.16	0.20	30.38
	150	9	Cal + Arg	93.69	7.25	40.42	5.62	0.77	22.38	3.09	0.16	0.16	30.40
	150	12	Cal + Arg	94.09	7.18	41.02	5.61	0.81	24.06	2.63	0.18	0.13	31.54
	150	15	Cal + Arg	92.99	7.14	41.40	5.63	0.84	26.44	1.36	0.19	0.07	31.89
	150	18	Cal + Arg	84.56	7.05	40.77	5.52	0.84	25.43	2.29	0.19	0.11	32.25
	150	21	Cal + Arg	96.24	6.97	40.90	5.55	0.86	25.00	2.17	0.18	0.10	32.07
	150	24	Cal + Arg	99.34	7.14	40.90	5.54	0.85	26.64	0.92	0.20	0.04	32.18
	150	27	Cal + Arg	88.49	7.22	40.44	5.42	0.85	24.28	2.58	0.18	0.12	32.85
	150	30	Cal + Arg	99.16	7.18	40.97	5.55	0.86	25.77	1.25	0.19	0.06	32.15
170_A	170	3	Cal + Arg	69.79	7.05	40.89	5.61	0.72	20.65	3.94	0.15	0.22	31.33
	170	6	Cal + Arg	75.97	6.91	40.84	5.37	0.78	24.55	2.30	0.19	0.12	34.10
	170	9	Cal + Arg	87.29	6.99	40.38	5.39	0.80	26.20	1.73	0.20	0.09	33.16
	170	12	Cal + Arg	92.82	6.95	40.91	5.25	0.84	26.43	1.37	0.21	0.07	35.78
	170	15	Cal + Arg	95.03	6.99	40.36	5.29	0.84	26.94	1.66	0.21	0.08	34.37
	170	18	Cal + Arg	99.80	6.98	40.34	5.40	0.85	25.84	1.51	0.19	0.07	32.97
	170	21	Cal + Arg	92.92	7.03	41.16	5.59	0.86	26.72	1.40	0.20	0.07	32.01
	170	24	Cal + Arg	97.92	7.02	40.80	5.41	0.85	27.31	1.34	0.21	0.06	33.60
	170	27	Cal + Arg	93.48	6.94	40.20	5.41	0.82	25.54	1.39	0.19	0.07	32.65
	170	30	Cal + Arg	99.23	7.11	40.32	5.29	0.85	27.33	1.07	0.21	0.05	34.28
98_B	98	7	Cal + Arg	46.92	7.36	41.72	6.57	0.77	13.88	5.37	0.09	0.29	21.20
	98	14	Cal + Arg	53.33	7.38	40.57	6.39	0.70	19.49	2.96	0.12	0.17	21.17
	98	21	Cal + Arg	50.83	7.31	41.09	6.33	0.76	17.00	3.89	0.11	0.21	22.81
	98	28	Cal + Arg	80.48	7.34	40.78	6.11	0.81	19.05	2.17	0.13	0.11	25.05
	98	35	Cal + Arg	78.19	7.38	40.92	3.59	0.48	11.23	1.72	0.13	0.15	56.03
	98	42	Cal + Arg	70.10	7.48	41.16	6.16	0.91	21.03	2.39	0.14	0.11	25.08
	98	49	Cal + Arg	87.62	7.46	41.81	6.20	0.93	20.63	1.53	0.14	0.07	25.75
130_B	130	4	Cal + Arg	53.90	7.04	41.79	6.04	0.75	19.61	3.87	0.14	0.22	27.63
	130	8	Cal + Arg	64.41	7.06	40.47	5.98	0.73	18.92	3.89	0.13	0.22	25.98
	130	12	Cal + Arg	89.74	7.11	41.52	5.77	0.89	24.59	2.01	0.18	0.09	30.37
	130	16	Cal + Arg	94.63	7.24	40.99	5.91	0.81	21.95	1.74	0.15	0.09	27.75
	130	20	Cal + Arg	91.33	7.00	40.74	5.85	0.84	23.70	1.86	0.16	0.09	28.08
	130	24	Cal + Arg	92.54	7.13	40.82	5.39	0.89	23.19	1.16	0.18	0.05	33.87
	130	28	Cal + Arg	91.10	7.16	40.15	5.70	0.89	23.26	0.80	0.16	0.04	28.91
	130	32	Cal + Arg	99.36	7.21	40.94	5.60	0.91	21.84	1.32	0.16	0.06	31.55
	130	36	Cal + Arg	99.20	7.13								
	130	40	Cal + Arg	98.67	7.25	41.40	6.01	0.92	24.28	1.69	0.17	0.08	27.31
150_B	150	3	Cal + Arg	68.40	7.10	41.52	5.90	0.75	19.80	4.95	0.14	0.27	28.83
	150	6	Cal + Arg	73.59	7.06	41.44	5.85	0.78	20.92	3.01	0.15	0.16	29.30
	150	9	Cal + Arg	78.86	7.16	41.31	5.64	0.83	23.38	2.11	0.17	0.10	31.59
	150	12	Cal + Arg	68.35	6.98	41.23	6.40	0.76	28.68	1.85	0.18	0.10	22.26
	150	15	Cal + Arg	96.98	7.00	40.33	5.37	0.84	21.72	1.73	0.16	0.08	33.32

Table 1 (continued)

Experimental ID	Temp (°C)	Duration (days)	Mineralogy by XRD	Calcite proportion (%)	pH(25°C)	Ca(mM)	Mg(mM)	Sr(mM)	(Mg/Ca)$_{solid}$ (mM/M)	(Sr/Ca)$_{solid}$ (mM/M)	D$_{Mg}$	D$_{Sr}$	Mg incorporation(%)
	150	18	Cal + Arg	96.29	7.15	40.75	5.86	0.88	24.39	2.15	0.17	0.10	28.02
	150	21	Cal + Arg	99.72	7.16	40.23	5.52	0.89	25.18	1.33	0.18	0.06	31.32
	150	24	Cal + Arg	98.61	7.27	40.59	6.77	0.88	29.62	1.50	0.18	0.07	16.50
	150	27	Cal + Arg	97.04	7.20	40.97	5.67	0.90	25.40	1.30	0.18	0.06	30.72
	150	30	Cal + Arg	98.37	7.18	41.00	5.68	0.91	25.25	1.51	0.18	0.07	30.66

Cal: calcite.
Arg: Aragonite.

2002; Zhu et al., 2021). Briefly, a set of standards with the different Mg and Sr (0.04 to 2.8 ppm) but the same Ca concentrations (20 ppm) were prepared, then the fitted line for Mg(Sr)/Ca ratio against intensity ratio data was calibrated. The Ca concentration in each test solution was adjusted to ~20 ppm before analysis. In addition, the standard-sample bracketing method was applied to correct the sensitivity drift for the ICP-OES. By using the above measures, the precision for Mg/Ca and Sr/Ca ratio measurement was better than ±2 %.

The pH measurements of solutions were performed at ambient conditions by Mettler Toledo combined electrode, which was calibrated by buffer standard solutions (pH = 4.01, 7.00, and 9.21 at 25 °C) with an uncertainty of 0.02 units. The PHREEQC software was used to calculate the speciation of aqueous solutions with its *llnl.-dat* database. The thermodynamic constants for oxalate dissociation (Gautier et al., 2015) and complexation with metal ions (Johnson et al., 1992; Prapaipong et al., 1999) were included in PHREEQC calculations.

2.4. Magnesium isotope analysis

Purification of Mg in the samples was achieved using a two-stage ion-exchange column chemistry procedure. The first stage of column chemistry followed a well-established method in the lab (Hu et al., 2017; Li et al., 2019). An aliquot of the sample containing approximately 20 µg Mg was first dissolved in 0.5 ml 1.5 N HNO$_3$ and the solution was loaded onto a quartz column with pre-cleaned 1 ml Biorad$^@$ cation exchange resin (AG50W-X12, 100 to 200 mesh). Then 1.5 N HNO$_3$ and 6 N HCl were used to elute the column to remove Na, Ca, Sr, and other cations from Mg. For the second stage of column chemistry, a column that contained 0.3 ml Eichrom DGA resin was used to remove the last vestige of Ca in the purified Mg, as reported by Li et al. (2012). Recovery of the Mg was > 97 %, and the total procedural blank for the chemical procedure was < 20 ng.

Magnesium isotope ratio measurements were performed on a Nu 1700 Sapphire MC-ICP-MS at Nanjing University. The instrument was operated in high energy (no collision cell) and wet plasma mode. Standard-sample-standard bracketing method was applied to correct for the instrument drift and mass bias. An in-house Mg solution (A-Mg), which has a δ^{26}Mg value of −3.25 ‰ relative to DSM3, was used as the bracketing standard. The Mg concentration of the samples matched that of the standard at a level of 0.50 ± 0.05 ppm. Solutions were introduced into the instrument using a 100 µL/min Glass Expansion nebulizer. The typical signal intensity was 7–10 V on ^{24}Mg (10^{11} Ω resistor). Each isotope analysis consisted of forty 4-second integrations, which yielded a typical internal precision of < 0.04 ‰ for ^{26}Mg/^{24}Mg ratios.

Magnesium isotope data are reported using the standard delta notation (‰) of δ^{26}Mg and δ^{25}Mg for the ^{26}Mg/^{24}Mg and ^{25}Mg/^{24}Mg ratios relative to the DSM3 Mg isotope standard, where

$$\delta^x Mg = \left[\left({}^x Mg / {}^{24} Mg_{sample} \right) / \left({}^x / {}^{24} Mg_{DSM3} \right) - 1 \right] \times 1000 \quad (1)$$

and the Mg isotope fractionation factor between two phases A and B is expressed as:

$$\Delta^x Mg_{A-B} = \delta^x Mg_A - \delta^x Mg_B \approx 10^3 ln\alpha_{A-B}^{x/24} \quad (2)$$

where x = 25 or 26.

The error in Mg isotope fractionation factors was calculated following the error propagation function:

$$Err\Delta Mg_{A-B} = \left[(Err\delta Mg_A)^2 + (Err\delta Mg_B)^2 \right]^{1/2} \quad (3)$$

The accuracy of Mg isotope measurements was verified by analyzing the pure Mg international standards (Cambridge1 and DSM3). Moreover, IAPSO standard seawater and two matrix-matching synthetic standard solutions (mixture of CaCl$_2$ and in-house Mg standard HPS932001 and HPS909104, 50:1 mol ratio for Ca: Mg) were processed as the unknown samples in the ion-exchange procedure. The measured Mg isotope compositions for both pure Mg standard solutions and standard samples (seawater and matrix-matching synthetic standard) match well with published values (i.e., δ^{26}Mg$_{Seawater}$ = −0.83 ± 0.12, Appendix Table S1). Based on repeated analyses of these standards and test solutions over multiple sessions over six months, the long external reproducibility for Mg isotopes was at a level of ±0.10 ‰ for δ^{26}Mg (Appendix Fig. S2).

3. Results

3.1. Mineralogy

The mineralogy of the solid experimental products and the chemical composition of the aqueous solutions are summarized in Table 1. Briefly, the solid phases in all experiments consisted only of aragonite and calcite (Table 1). In all experiments, the proportion of calcite increased with increasing reaction time (Fig. 1) and the rate of aragonite-to-calcite transformation increased with higher temperatures. The proportion of calcite in the solid product was around 40 % after 7 days of reaction at 98 °C, whereas it took 4 days for experiments at 130 °C to reach a similar proportion of calcite. For experiments at 170 °C, 70 % of aragonite was transformed to calcite after 3 days of reaction. Moreover, a higher oxalate concentration generally led to higher aragonite conversion rates at the same temperature (e.g., Fig. 1C).

Under SEM, the starting aragonite occurs as aggregates of platy crystals, a typical biological structure (Fig. 2). After hydrothermal experiments, the solid products transformed to homogeneous calcite with anhedral but granular morphology. The grain size of calcite was 1–5 µm irrespective of reaction temperature for all experiments (Fig. 2). There was a subtle, but noticeable increase in the size of calcite grains with increasing reaction time (Fig. 2).
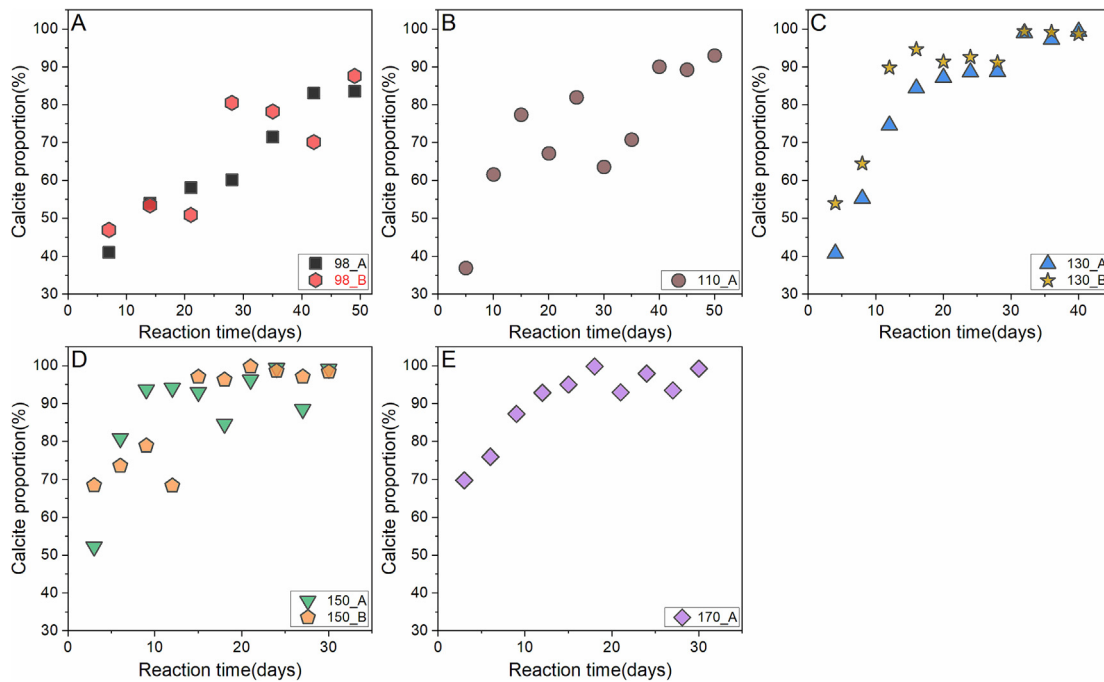
Fig. 1. The proportion of calcite in the solid phase versus reaction time for different experiments.
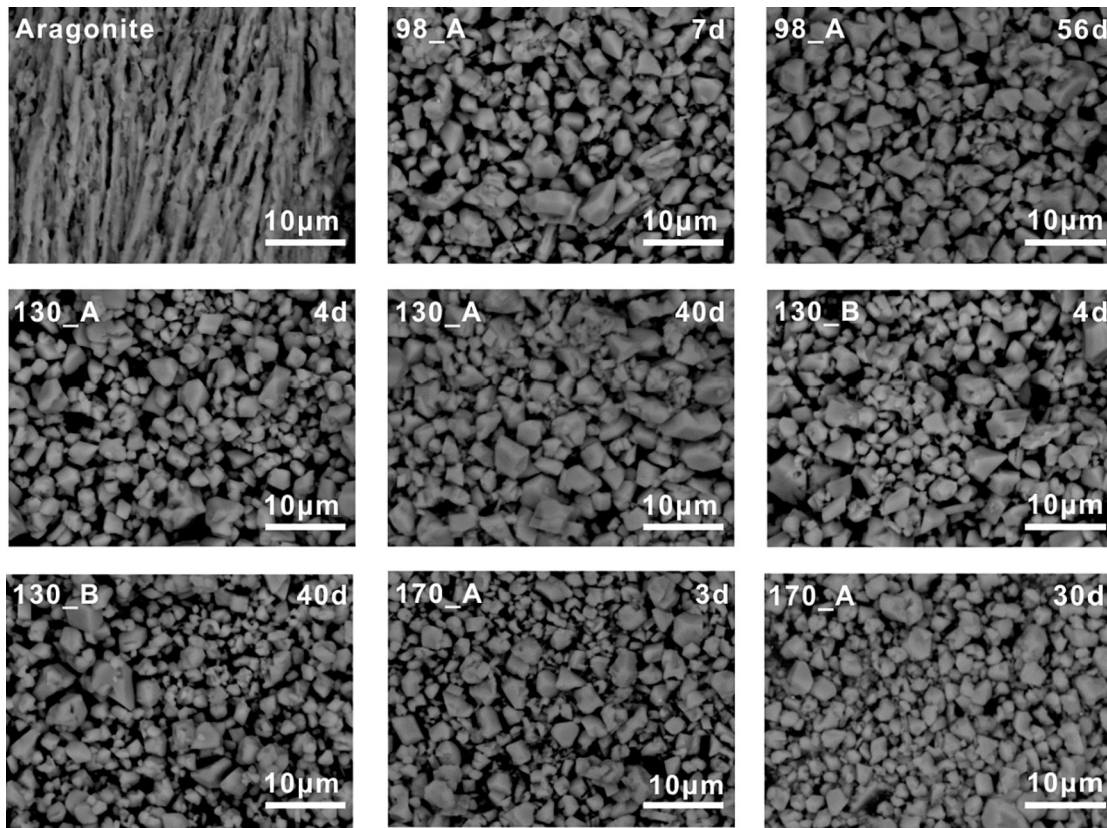

Fig. 2. The SEM images of starting aragonite and calcite products after conversion experiments.

3.2. Elemental partitioning

The Mg and Sr concentrations for bulk solid samples ranged from 1.10 to 2.87 mol% and 0.08 to 0.66 mol%, respectively. The apparent elemental partition coefficient (D) was calculated based on the molar ratios of (mM/M) for the elements between the solid product and the aqueous solution:

$$D_{Mg} = (Mg/Ca)_{solid}/(Mg/Ca)_{soln} \qquad (4)$$
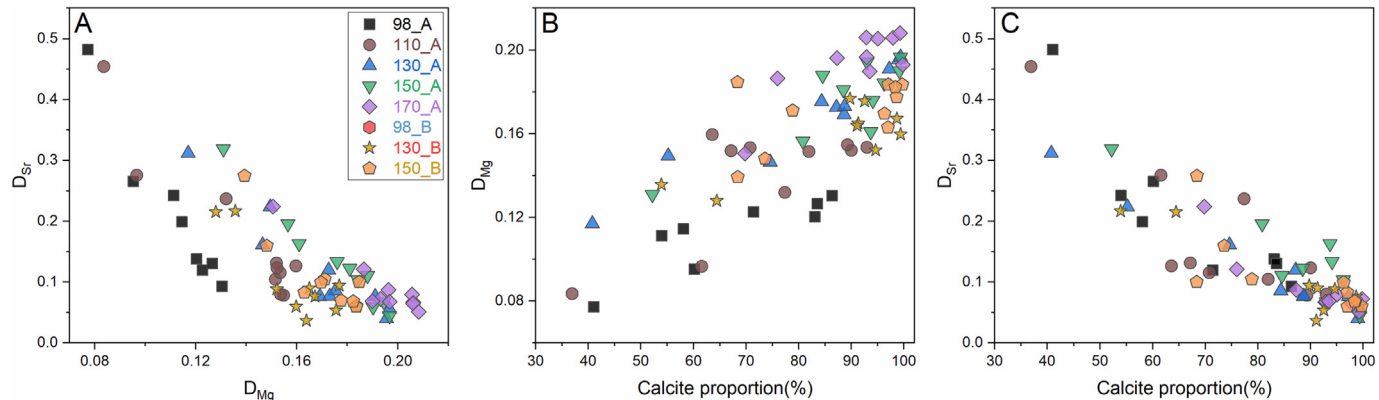
Fig. 3. (A) Plot of D_{Mg} versus D_{Sr} for all experiments in this study; (B) Plot of D_{Mg} versus calcite proportion (%) for all experiments in this study, symbols are the same with plot A; (C) Plot of D_{Sr} versus calcite proportion (%) for all experiments in this study, symbols are the same with plot A.

$$D_{Sr} = (Sr/Ca)_{solid}/(Sr/Ca)_{soln} \qquad (5)$$

The D_{Mg} values increased at the early stage of the experiments, then remained relatively constant for all experiment series (Table 1, Appendix Fig. S3). In contrast, the D_{Sr} values decreased for all experiment series and then remained constant (Table 1, Appendix Fig. S4). Notably, the apparent D_{Mg} and D_{Sr} values show negative correlations for all experiment series (Fig. 3A).

3.3. Magnesium isotope fractionation

The starting aragonite and aqueous Mg (in both solution A and solution B) had δ^{26}Mg values of $-1.90‰$ and $-1.10‰$, respectively (Table 2). The aqueous solutions after the reactions all had higher ^{26}Mg/^{24}Mg ratios as compared to the starting solution, while the solid phases had lower δ^{26}Mg values than that of starting aragonite. Moreover, the δ^{26}Mg values of both solid and aqueous phases stabilized with a longer reaction time (Fig. 4).

The apparent Mg isotope fractionation factors between bulk solids and aqueous solutions (Δ^{26}Mg$_{solid-soln}$) range from ca. $-1.84‰$ at 98 °C (Exp. 98_B) to ca. $-1.35‰$ (Exp. 170_A) at 170 °C, showing a strong positive correlation with the reaction temperatures (Fig. 5). For experiments at the same temperature, the Δ^{26}Mg$_{solid-soln}$ values in experiment series B are slightly more negative on average compared to those in experiment series A (Fig. 6), indicating slightly greater magnitude Mg isotope fractionation in experiments with higher oxalate concentrations in the aqueous solutions.

4. Discussion

4.1. Partitioning of magnesium and strontium between calcite and aqueous solutions

In this study, the transformation of aragonite to calcite led to increasing apparent D_{Mg} values and decreasing apparent D_{Sr} values (Table 1). There is a positive correlation between the apparent D_{Mg} values and the calcite proportions in the bulk solids, as well as a negative correlation between D_{Sr} and calcite proportion (Fig. 3B, C). These correlations indicate the mixing of aragonite and calcite in the experimental products. Due to the difference in ionic radii between Mg (Sr) and Ca (Shannon, 1976), Mg is more compatible with the lattice of calcite than aragonite, whereas Sr is more compatible with aragonite than calcite (Morse and Mackenzie, 1990; Morse et al., 2007).

Numerous experimental studies have been conducted to investigate the partitioning behavior of Mg and Sr between calcite and aqueous solutions (e.g., Lorens, 1981; Mucci and Morse, 1983; Dietzel and Usdowski, 1996; Tang et al., 2008b; Mavromatis et al., 2013; Goetschl et al., 2019), and these studies may be grouped into two types. One type is the direct precipitation of calcite from aqueous solutions (e.g., Pingitore and Eastman, 1986; Zhong and Mucci, 1989; Tang et al., 2012; Gabitov et al., 2014; Mavromatis et al., 2017a). Several studies have shown that the distribution coefficients could be significantly influenced by the calcite precipitation rate (Lorens, 1981; Tesoriero and Pankow, 1996; Nehrke et al., 2007; Tang et al., 2008b; Tang et al., 2012; Mavromatis et al., 2013; Gabitov et al., 2014; Goetschl et al., 2019; Gabitov et al., 2021), implying kinetic effects associated with direct mineral precipitation. Another type is the transformation of aragonite (Katz et al., 1972; Katz, 1973; Jacobson and Usdowski, 1976; Baker et al., 1982; Humphrey and Howell, 1999; Malone and Baker, 1999) or dolomite (Jacobson and Usdowski, 1976; Stoessell et al., 1987; Malone and Baker, 1999) to calcite, as the approach taken here. Previous studies on the hydrothermal alteration of aragonite showed that the formation of calcite was favored at low rates of replacement and led to the extensive elemental exchange between fluids and minerals (Pederson et al., 2019; Pederson et al., 2020). Therefore, the relatively slow calcite formation rates that accompany these transformation reactions are thought to better mimic slow precipitation from solution, which could result in elemental distribution closer to equilibrium (Malone and Baker, 1999). In addition, it has been proposed that equilibrium elemental distribution data could be obtained by studying deep-sea carbonate sediments, which had experienced extensive recrystallization in pore fluids (Lammers and Mitnick, 2019; Zhang and DePaolo, 2020).

We compile the Mg and Sr distribution coefficient data in literature in Fig. 7, in which the average $D_{Mg}(D_{Sr})$ values for > 90 % calcite conversion in this study are also plotted for comparison. All the direct precipitation experiments were conducted at relatively low temperatures (Gascoyne, 1983; Mucci and Morse, 1983; Mucci, 1986; Howson et al., 1987; Mucci, 1987; Oomori et al., 1987; Zhong and Mucci, 1989; Burton and Walter, 1991; Hartley and Mucci, 1996; Huang et al., 2001; Day and Henderson, 2013; Mavromatis et al., 2013; Gabitov et al., 2014; Mavromatis et al., 2017a; Drysdale et al., 2019), while Katz (1973) applied the aragonite transition experiments from 25 to 90 °C. We note that D_{Mg} values obtained in this study and those in the study of Katz (1973) define a good correlation with temperature (Fig. 7A), where the higher-temperature results obtained here broadly lie on an extrapolation of the lower temperature results of Katz (1973).

The direct precipitation of calcite produced variable D_{Sr} values (Holland et al., 1964; Lorens, 1981; Mucci and Morse, 1983;

Table 2
Mg isotope data of solution and solid phases in experiments.

Experimental ID	Temp (°C)	Duration (days)	Solution (‰)					Solid (‰)					Fractionation (solid-solution)			
			$\delta^{26/24}$Mg	2SD	$\delta^{25/24}$Mg	2SD	n(N)[1]	$\delta^{26/24}$Mg	2SD	$\delta^{25/24}$Mg	2SD	n(N)[1]	$\Delta^{26/24}$Mg	2SD[2]	$\Delta^{25/24}$Mg	2SD[2]
Starting Aragonite								−1.90	0.05	−0.97	0.03	8(2)				
Starting Solution			−1.10	0.10	−0.57	0.06	14(3)									
seawater			−0.83	0.12	−0.42	0.10	21(7)									
SolutionA1[3]			−0.69	0.10	−0.36	0.06	48(16)									
SolutionA2[4]			−2.96	0.10	−1.52	0.06	46(13)									
98_A	98	7	−0.76	0.03	−0.39	0.03	4(1)	−2.45	0.07	−1.26	0.03	4(1)	−1.70	0.08	−0.87	0.04
	98	14	−0.72	0.05	−0.37	0.04	4(1)	−2.45	0.08	−1.26	0.03	4(1)	−1.73	0.09	−0.89	0.05
	98	21	−0.69	0.03	−0.36	0.03	4(1)	−2.42	0.08	−1.25	0.04	4(1)	−1.73	0.09	−0.91	0.05
	98	28	−0.71	0.03	−0.37	0.03	4(1)	−2.47	0.04	−1.27	0.02	4(1)	−1.75	0.05	−0.94	0.04
	98	35	−0.69	0.05	−0.35	0.03	4(1)	−2.39	0.05	−1.23	0.02	4(1)	−1.70	0.07	−0.87	0.03
	98	42	−0.63	0.05	−0.32	0.06	4(1)	−2.39	0.05	−1.23	0.05	4(1)	−1.76	0.07	−0.93	0.08
	98	49	−0.58	0.06	−0.30	0.02	4(1)	−2.37	0.05	−1.22	0.01	4(1)	−1.79	0.08	−0.95	0.02
110_A	110	5	−0.75	0.05	−0.39	0.02	4(1)	−2.30	0.07	−1.18	0.03	4(1)	−1.55	0.08	−0.81	0.04
	110	10	−0.63	0.08	−0.32	0.04	4(1)	−2.21	0.02	−1.14	0.01	4(1)	−1.59	0.08	−0.80	0.05
	110	15	−0.68	0.06	−0.35	0.02	4(1)	−2.23	0.07	−1.15	0.06	4(1)	−1.55	0.09	−0.78	0.07
	110	20	−0.55	0.07	−0.29	0.04	4(1)	−2.22	0.07	−1.15	0.06	4(1)	−1.67	0.10	−0.88	0.07
	110	25	−0.57	0.04	−0.29	0.04	4(1)	−2.27	0.05	−1.17	0.06	4(1)	−1.71	0.06	−0.89	0.07
	110	30	−0.62	0.03	−0.32	0.02	4(1)	−2.25	0.06	−1.15	0.05	4(1)	−1.63	0.06	−0.85	0.06
	110	35	−0.63	0.04	−0.32	0.01	4(1)	−2.33	0.05	−1.20	0.01	4(1)	−1.70	0.06	−0.88	0.02
	110	40	−0.65	0.07	−0.33	0.06	4(1)	−2.31	0.07	−1.19	0.03	4(1)	−1.65	0.10	−0.85	0.06
	110	45	−0.62	0.05	−0.32	0.02	4(1)	−2.31	0.04	−1.19	0.04	4(1)	−1.69	0.06	−0.88	0.04
	110	50	−0.61	0.04	−0.31	0.04	4(1)	−2.36	0.08	−1.21	0.03	4(1)	−1.75	0.09	−0.91	0.05
130_A	130	4	−0.66	0.05	−0.34	0.02	4(1)	−2.16	0.01	−1.12	0.01	4(1)	−1.50	0.05	−0.76	0.03
	130	8	−0.64	0.07	−0.33	0.01	4(1)	−2.16	0.06	−1.11	0.02	4(1)	−1.52	0.09	−0.81	0.02
	130	12	−0.60	0.09	−0.30	0.04	4(1)	−2.24	0.05	−1.16	0.00	4(1)	−1.65	0.10	−0.84	0.04
	130	16	−0.55	0.07	−0.28	0.07	4(1)	−2.19	0.09	−1.12	0.04	4(1)	−1.64	0.11	−0.88	0.08
	130	20	−0.53	0.07	−0.27	0.03	4(1)	−2.20	0.05	−1.13	0.02	4(1)	−1.66	0.08	−0.88	0.04
	130	24	−0.50	0.02	−0.26	0.00	4(1)	−2.11	0.02	−1.08	0.01	4(1)	−1.61	0.03	−0.84	0.01
	130	28	−0.61	0.04	−0.31	0.03	4(1)	−2.14	0.09	−1.10	0.05	4(1)	−1.53	0.09	−0.81	0.06
	130	32	−0.50	0.07	−0.25	0.03	4(1)	−2.12	0.03	−1.09	0.03	4(1)	−1.62	0.08	−0.84	0.05
	130	36	−0.54	0.07	−0.28	0.02	4(1)	−2.15	0.03	−1.11	0.04	4(1)	−1.61	0.08	−0.86	0.05
	130	40	−0.51	0.05	−0.26	0.03	4(1)	−2.10	0.04	−1.08	0.05	4(1)	−1.58	0.07	−0.82	0.05
150_A	150	3	−0.65	0.06	−0.34	0.05	4(1)	−2.09	0.05	−1.07	0.02	4(1)	−1.44	0.08	−0.75	0.05
	150	6	−0.62	0.04	−0.31	0.02	4(1)	−2.14	0.07	−1.10	0.05	4(1)	−1.52	0.08	−0.79	0.06
	150	9	−0.60	0.05	−0.31	0.01	4(1)	−2.09	0.08	−1.07	0.05	4(1)	−1.48	0.09	−0.78	0.05
	150	12	−0.58	0.05	−0.30	0.01	4(1)	−2.12	0.10	−1.09	0.05	4(1)	−1.54	0.12	−0.79	0.06
	150	15	−0.57	0.05	−0.29	0.04	4(1)	−2.06	0.07	−1.06	0.02	4(1)	−1.49	0.09	−0.79	0.04
	150	18	−0.57	0.05	−0.29	0.04	4(1)	−2.08	0.08	−1.08	0.08	4(1)	−1.51	0.10	−0.75	0.10
	150	21	−0.57	0.07	−0.30	0.05	4(1)	−2.03	0.09	−1.05	0.07	4(1)	−1.45	0.12	−0.76	0.09
	150	24	−0.56	0.04	−0.29	0.03	4(1)	−2.12	0.06	−1.09	0.04	4(1)	−1.56	0.07	−0.82	0.05
	150	27	−0.57	0.06	−0.29	0.03	4(1)	−2.06	0.03	−1.06	0.01	4(1)	−1.49	0.07	−0.75	0.04
	150	30	−0.55	0.05	−0.29	0.02	4(1)	−2.08	0.08	−1.07	0.05	4(1)	−1.53	0.10	−0.81	0.05
170_A	170	3	−0.61	0.05	−0.32	0.01	4(1)	−2.00	0.09	−1.03	0.05	4(1)	−1.39	0.10	−0.75	0.05
	170	6	−0.60	0.03	−0.31	0.03	4(1)	−1.96	0.08	−1.00	0.06	4(1)	−1.36	0.08	−0.70	0.07
	170	9	−0.58	0.05	−0.30	0.04	4(1)	−1.99	0.05	−1.03	0.04	4(1)	−1.40	0.07	−0.72	0.05
	170	12	−0.55	0.04	−0.29	0.04	4(1)	−1.97	0.03	−1.02	0.03	4(1)	−1.43	0.05	−0.74	0.06
	170	15	−0.59	0.06	−0.31	0.02	4(1)	−2.00	0.05	−1.04	0.03	4(1)	−1.41	0.07	−0.75	0.04
	170	18	−0.60	0.04	−0.30	0.05	4(1)	−1.99	0.08	−1.02	0.09	4(1)	−1.39	0.09	−0.71	0.10
	170	21	−0.60	0.04	−0.31	0.04	4(1)	−2.04	0.05	−1.05	0.04	4(1)	−1.44	0.07	−0.72	0.06
	170	24	−0.56	0.09	−0.29	0.06	4(1)	−2.00	0.01	−1.03	0.02	4(1)	−1.43	0.09	−0.75	0.06
	170	27	−0.62	0.09	−0.32	0.05	4(1)	−2.04	0.07	−1.05	0.05	4(1)	−1.41	0.11	−0.75	0.07
	170	30	−0.62	0.03	−0.32	0.05	4(1)	−1.98	0.05	−1.02	0.03	4(1)	−1.35	0.06	−0.70	0.06
98_B	98	7	−0.59	0.09	−0.30	0.02	4(1)	−2.40	0.02	−1.24	0.03	4(1)	−1.81	0.09	−0.92	0.04
	98	14	−0.62	0.08	−0.32	0.05	4(1)	−2.41	0.04	−1.25	0.05	4(1)	−1.79	0.09	−0.98	0.07
	98	21	−0.61	0.05	−0.32	0.03	4(1)	−2.41	0.06	−1.24	0.07	4(1)	−1.80	0.07	−0.95	0.08
	98	28	−0.59	0.04	−0.31	0.02	4(1)	−2.41	0.04	−1.24	0.02	4(1)	−1.82	0.06	−0.96	0.03
	98	35	−0.69	0.07	−0.36	0.03	4(1)	−2.48	0.03	−1.28	0.03	4(1)	−1.79	0.07	−0.93	0.04
	98	42	−0.60	0.06	−0.31	0.06	4(1)	−2.44	0.03	−1.26	0.01	4(1)	−1.84	0.07	−0.94	0.06
	98	49	−0.59	0.06	−0.30	0.03	4(1)	−2.36	0.05	−1.21	0.04	4(1)	−1.78	0.08	−0.93	0.05
130_B	130	4	−0.65	0.01	−0.33	0.04	4(1)	−2.28	0.07	−1.17	0.04	4(1)	−1.62	0.07	−0.86	0.06
	130	8	−0.64	0.05	−0.33	0.05	4(1)	−2.39	0.07	−1.23	0.09	4(1)	−1.75	0.08	−0.95	0.10
	130	12	−0.55	0.05	−0.28	0.02	4(1)	−2.19	0.00	−1.13	0.02	4(1)	−1.64	0.05	−0.86	0.03
	130	16	−0.61	0.02	−0.32	0.06	4(1)	−2.33	0.03	−1.20	0.03	4(1)	−1.72	0.04	−0.90	0.07
	130	20	−0.61	0.07	−0.32	0.08	4(1)	−2.34	0.02	−1.20	0.03	4(1)	−1.73	0.07	−0.90	0.08
	130	24	−0.59	0.04	−0.30	0.02	4(1)	−2.20	0.06	−1.13	0.03	4(1)	−1.61	0.07	−0.88	0.04
	130	28	−0.58	0.02	−0.30	0.02	4(1)	−2.26	0.07	−1.17	0.03	4(1)	−1.68	0.07	−0.88	0.04
	130	32	−0.55	0.05	−0.28	0.04	4(1)	−2.31	0.04	−1.19	0.01	4(1)	−1.76	0.06	−0.95	0.04
	130	36														
	130	40	−0.62	0.02	−0.32	0.04	4(1)	−2.15	0.02	−1.11	0.03	4(1)	−1.53	0.03	−0.82	0.05

(*continued on next page*)

Table 2 (*continued*)

Experimental ID	Temp (°C)	Duration (days)	Solution (‰)					Solid (‰)					Fractionation (solid-solution)			
			$\delta^{26/24}$Mg	2SD	$\delta^{25/24}$Mg	2SD	n(N)[1]	$\delta^{26/24}$Mg	2SD	$\delta^{25/24}$Mg	2SD	n(N)[1]	$\Delta^{26/24}$Mg	2SD[2]	$\Delta^{25/24}$Mg	2SD[2]
150_B	150	3	−0.72	0.08	−0.37	0.05	4(1)	−2.19	0.06	−1.13	0.03	4(1)	−1.47	0.10	−0.78	0.06
	150	6	−0.66	0.03	−0.34	0.04	4(1)	−2.14	0.02	−1.10	0.03	4(1)	−1.48	0.03	−0.78	0.05
	150	9	−0.65	0.02	−0.33	0.02	4(1)	−2.17	0.05	−1.12	0.07	4(1)	−1.52	0.06	−0.79	0.07
	150	12	−0.64	0.03	−0.33	0.01	4(1)	−2.19	0.03	−1.13	0.02	4(1)	−1.54	0.04	−0.80	0.02
	150	15	−0.60	0.03	−0.30	0.02	4(1)	−2.21	0.08	−1.14	0.05	4(1)	−1.61	0.08	−0.89	0.06
	150	18	−0.70	0.05	−0.35	0.03	4(1)	−2.23	0.06	−1.14	0.05	4(1)	−1.53	0.08	−0.80	0.06
	150	21	−0.60	0.05	−0.31	0.03	4(1)	−2.21	0.08	−1.14	0.05	4(1)	−1.61	0.09	−0.85	0.06
	150	24	−0.57	0.10	−0.29	0.04	4(1)	−2.21	0.08	−1.14	0.05	4(1)	−1.64	0.12	−0.82	0.06
	150	27	−0.66	0.08	−0.34	0.02	4(1)	−2.21	0.02	−1.14	0.03	4(1)	−1.54	0.09	−0.81	0.03
	150	30	−0.62	0.05	−0.32	0.05	4(1)	−2.15	0.05	−1.11	0.03	4(1)	−1.53	0.07	−0.82	0.06

1. n denotes the total number of isotope analysis, N denotes the number of replicate.
2. ErrΔ^xMg = [(Errδ^xMg$_{solid}$)^2 + (Errδ^xMg$_{soln}$)^2]$^{1/2}$, x = 26 or 25.
3. Test solution contains 0.8 µmol of Mg (HPS909104, δ^{26}Mg = -0.67 ± 0.10 ‰ by Li et al., 2011) and 40 µmol of CaCl$_2$.
4. Test solution contains 0.8 µmol of Mg (HPS932001, δ^{26}Mg = -2.93 ± 0.14 ‰ by Li et al., 2011) and 40 µmol of CaCl$_2$.

Mucci, 1986; Pingitore and Eastman, 1986; Tesoriero and Pankow, 1996; Huang and Fairchild, 2001; Wasylenki et al., 2005; Gabitov and Watson, 2006; Nehrke et al., 2007; Tang et al., 2008b; Tang et al., 2012; Day and Henderson, 2013; Gabitov et al., 2014; AlKhatib and Eisenhauer, 2017; Drysdale et al., 2019), which are higher than equilibrium D$_{Sr}$ proposed by Zhang and DePaolo (2020) (Fig. 7B). In contrast, our results together with previously reported aragonite/dolomite transformation experimental data
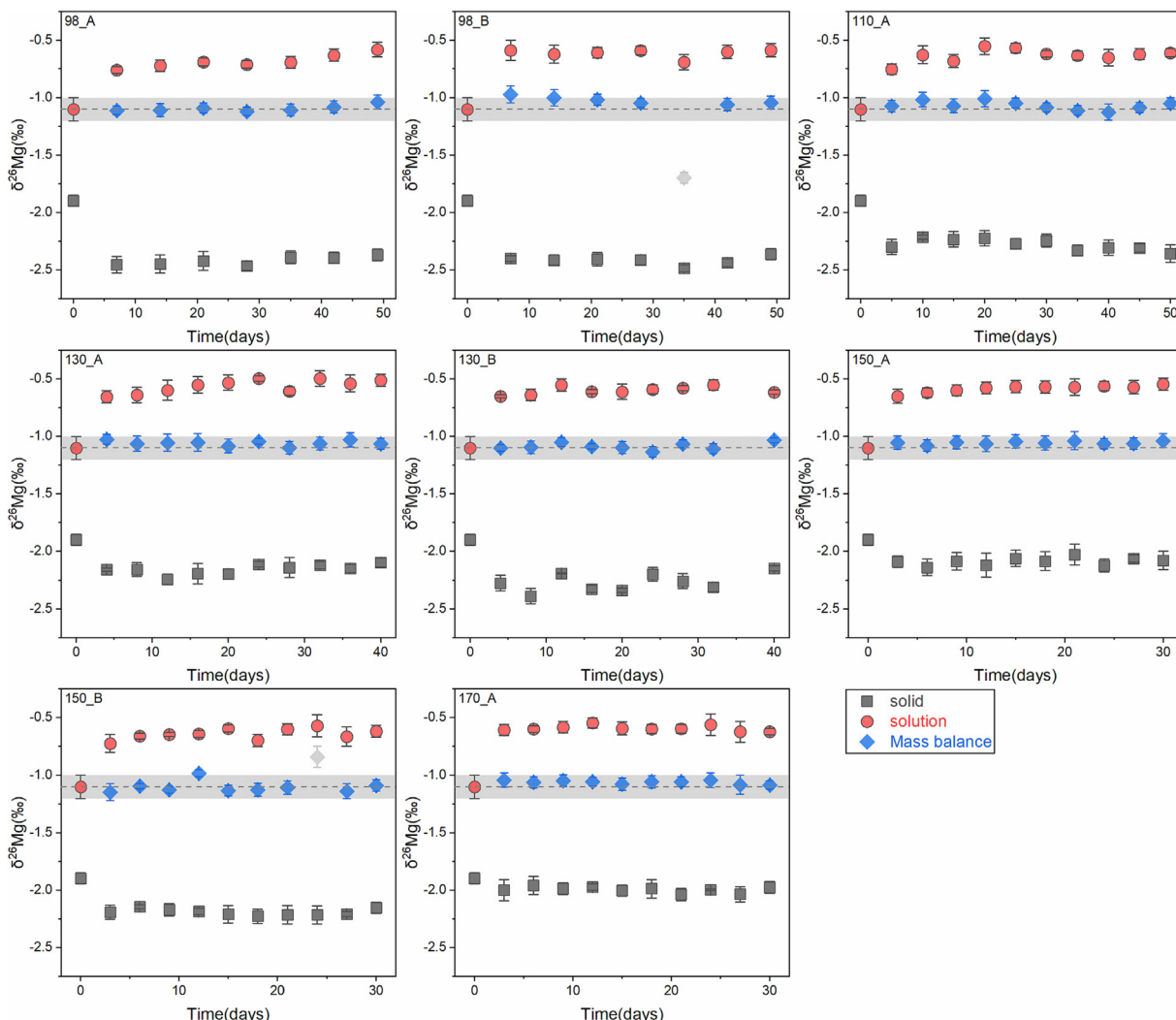
Fig. 4. The evolution of Mg isotopic composition (δ^{26}Mg) of solid and aqueous solutions, as well as the Mg isotope mass balances for each of the experiments. The shaded area represents the 2SD of the multiple analyses of the starting solutions. Gray diamond symbols in the plot (98_B and 150_B) denote anomalous mass balance calculation results, which were related to errors in Mg concentration measurements (or solution preparation) that cannot be traced back or corrected, we emphasize that such errors do not affect discussions on Mg isotope fractionations.
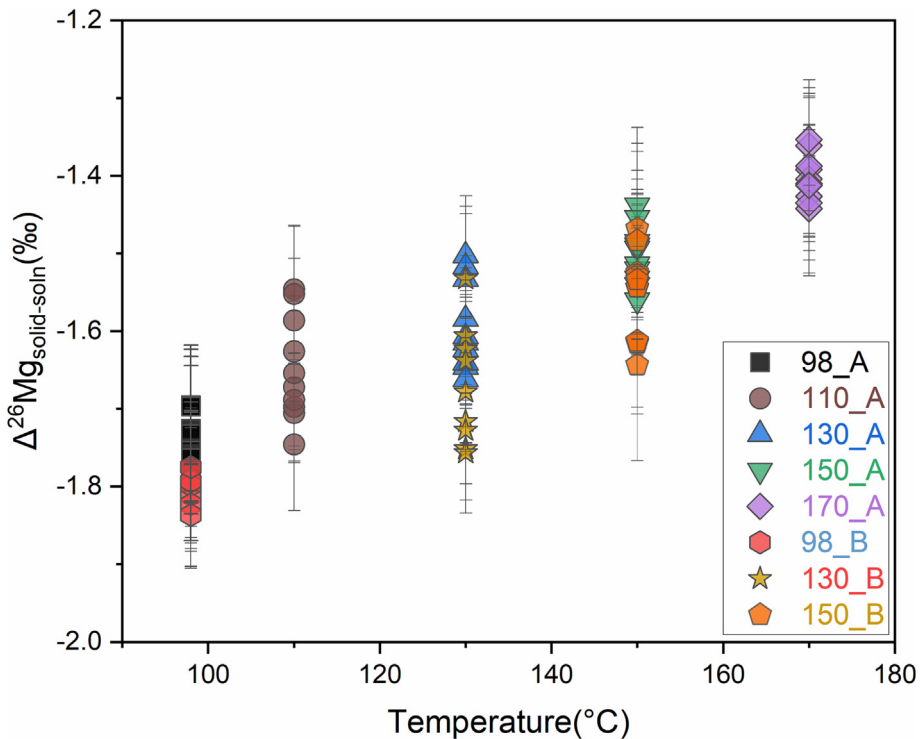
Fig. 5. The apparent Mg isotope fractionation factors between solid and aqueous phases ($\Delta^{26}Mg_{solid-soln}$) versus reaction temperature for all experiments.
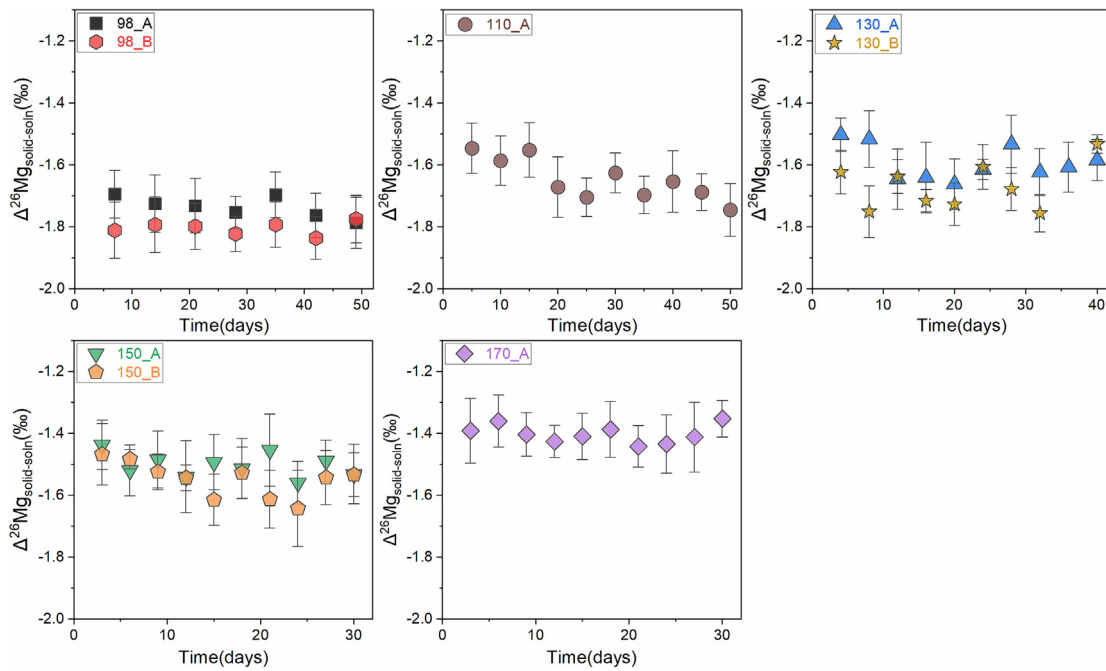
Fig. 6. The plot of bulk Mg isotope fractionation factors ($\Delta^{26}Mg_{solid-soln}$) between solid and aqueous solution versus time at the five experimental temperatures.

(Katz et al., 1972; Baker et al., 1982; Stoessell et al., 1987; Humphrey and Howell, 1999; Malone and Baker, 1999) are closer to the proposed equilibrium line by Zhang and DePaolo (2020).

Besides temperature, organic matter may influence element distributions. Mavromatis et al. (2017a) observed a significant enhancement of Mg uptake into calcite with the presence of several carboxyl-containing organic ligands including acetic acid,

citric acid, glutamic acid, salicylic acid, glycine, and EDTA. In this study, experiments with different oxalate concentrations (0.1 mM vs 1 mM) were conducted at 98, 130, and 150 °C. The higher D_{Mg} and lower D_{Sr} values were obtained at the early stage of the reaction for the experiments with higher oxalate concentration (Appendix Fig. S3, S4), but it should be attributed to the higher calcite proportion, as discussed earlier. With a longer reaction
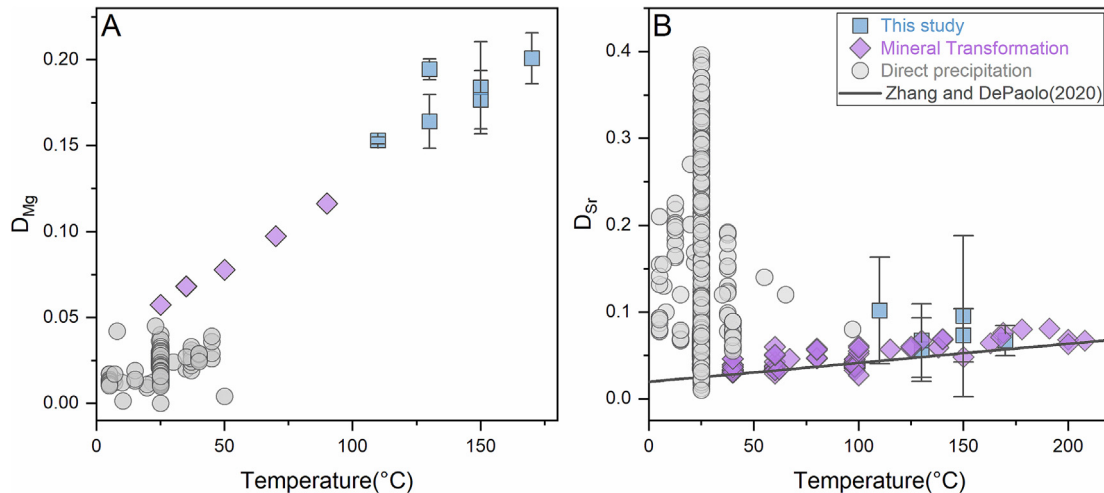
Fig. 7. Comparison of the D_{Mg} and D_{Sr} data obtained in this study and those reported for calcite in literature. (A) D_{Mg} versus temperature. (B) D_{Sr} versus temperature.

time, however, the D_{Mg} and D_{Sr} values became consistent among experiments with different oxalate concentrations at the same temperatures. Therefore, in our experiments, the oxalate appeared to have limited influence on Mg/Sr partition behavior, which was different from the effects of other carboxyl-containing organic ligands reported by Mavromatis et al. (2017a). This difference could be due to the higher reaction temperature in this study or the different formation pathways for calcite (conversion from aragonite versus direct precipitation).

4.2. Magnesium isotope fractionation between calcite and aqueous Mg^{2+}

The presence of more oxalate contributed to slightly lower $\Delta^{26}Mg_{solid-soln}$ values, that the weighted average $\Delta^{26}Mg_{solid-soln}$ values for experimental series 98_A, 130_A and 150_A with 0.1 mM of oxalates were -1.74 ± 0.03 ‰, -1.59 ± 0.04 ‰, and -1.50 ± 0.03 ‰, respectively, whereas for experimental series 98_B, 130_B and 150_B with 1 mM of oxalates, these values decrease to -1.80 ± 0.03 ‰, -1.64 ± 0.07 ‰, and -1.52 ± 0.03 ‰, respectively (Fig. 6). According to Schott et al. (2016), dissolved oxalate has chelating effects on Mg ions in aqueous solution, and the Mg-oxalate strongly enriches heavy Mg isotopes relative to free Mg-aquo ions (i.e., $Mg(H_2O)_6^{2+}$). Thus, experiments with higher dissolved oxalates yielded lower $\Delta^{26}Mg_{cal-soln}$ values given the same temperature. To account for the isotopic effect of Mg-oxalate in the experiments, we first calculated the speciation of Mg in aqueous solutions for all the experiments using PHREEQC. The results (Appendix Table S2) are plotted in Fig. 8, which shows that the mole fraction of free Mg-aquo ions decreases with increasing temperatures, while that of other Mg species increases with increasing temperature (Fig. 8A). When the concentration of oxalate increased to 1 mM, the mole fraction of Mg-oxalate increased by an order of magnitude (Fig. 8B). Based on isotope mass balance, the $\delta^{26}Mg$ values of aqueous Mg species can be calculated by:

$$\delta^{26}Mg_{soln} = \sum_i \left(F_i \times \delta^{26}Mg_i \right) \qquad (6)$$

where F_i represents the mole fraction of the ith Mg^{2+} species and $\delta^{26}Mg_i$ refers to the $\delta^{26}Mg$ values of the ith Mg^{2+} species, respectively.

Using equation (6), as well as the results of Mg speciation calculation and the Mg isotope fractionation factors between different

Mg species (Schott et al., 2016), the Mg isotope composition of free Mg-aquo ions (i.e., $Mg(H_2O)_6^{2+}$) for each experiment was calculated (Appendix Table S2). While the solid phase contained both starting aragonite and newly formed calcite, the Mg isotope composition of the solid phase can be expressed as:

$$\delta^{26}Mg_{solid} = F_{Cal} \times \delta^{26}Mg_{Cal} + F_{Ara} \times \delta^{26}Mg_{Ar} \qquad (7)$$

where F_{Cal} and F_{Ara} represent the fraction of Mg in calcite and aragonite, respectively; and $\delta^{26}Mg_{Cal}$ and $\delta^{26}Mg_{Ara}$ refer to the $\delta^{26}Mg$ values of calcite and aragonite, respectively. The Mg isotope composition of calcite may be obtained by assuming that there is no Mg isotope exchange between aragonite and aqueous solutions, where this assumption is based on the likely dissolution-reprecipitation process involved during the transformation of aragonite to calcite (see next section). This calculation produces a Mg isotope fractionation factor between calcite and a free Mg-aquo ions ($\Delta^{26}Mg_{cal-Mg^{2+}(aq)}$), as shown in Appendix Table S2. As plotted in Fig. 9, the $\Delta^{26}Mg_{cal-Mg^{2+}(aq)}$ values are identical within the analytical error for experiments at the same reaction temperature but with different oxalate concentrations.

4.3. Magnesium isotope fractionation behavior

The morphological differences between starting aragonite and produced calcite indicate that aragonite-to-calcite conversion took place via a dissolution-and-reprecipitation mechanism (Bischoff and Fyfe, 1968). During such a process, the dissolution of aragonite released its structural Mg that had a $\delta^{26}Mg$ of -1.90 ‰ into the solution. Based on the Mg content and mass of the aragonite, the dissolution of aragonite only contributed approximately 3 % of the total Mg in the aqueous solution, which had a negligible influence on the isotopic composition of the solution.

Precipitation of calcite preferentially removed light Mg isotopes (e.g., Saenger and Wang, 2014) from the solution, and the Mg isotope effect of this is seen early in the Mg isotope compositions of the solutions (Fig. 4). We may describe the calcite-solution Mg isotope fractionation by a Rayleigh-type process or batch equilibrium process. In a batch equilibrium model, it is assumed that the solid and aqueous phases are always in isotope equilibrium. In a Rayleigh model, however, it is assumed that once calcite is precipitated from the solution, calcite no longer exchanges with the aqueous solution, although the instantaneous precipitation process could follow equilibrium isotope fractionation. The evolution of the
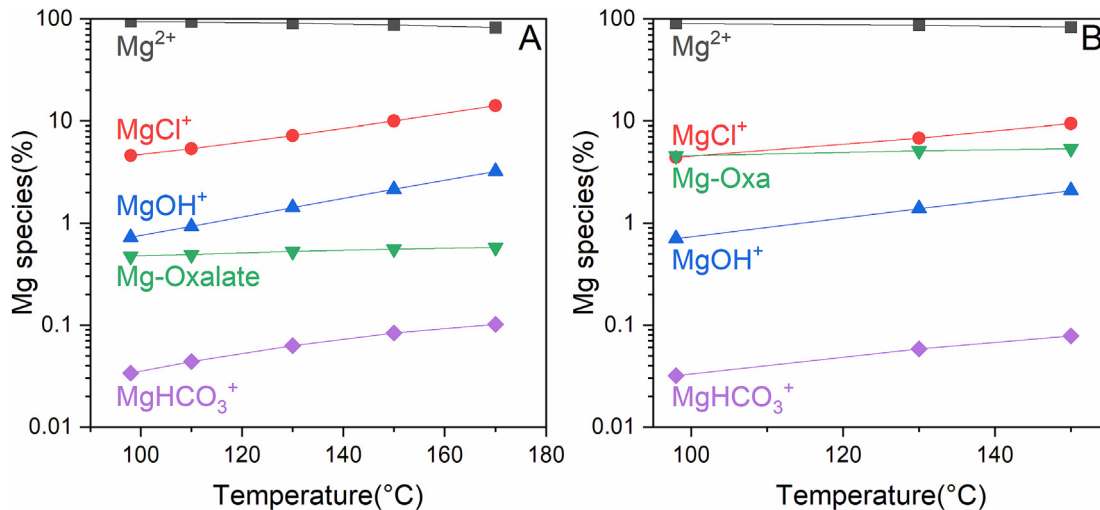
Fig. 8. The mole fraction of each Mg^{2+} species for aqueous solutions, calculated using PHREEQC. (A) Experiment series with 0.1 mM of oxalate, (B) Experiment series with 1 mM of oxalate.
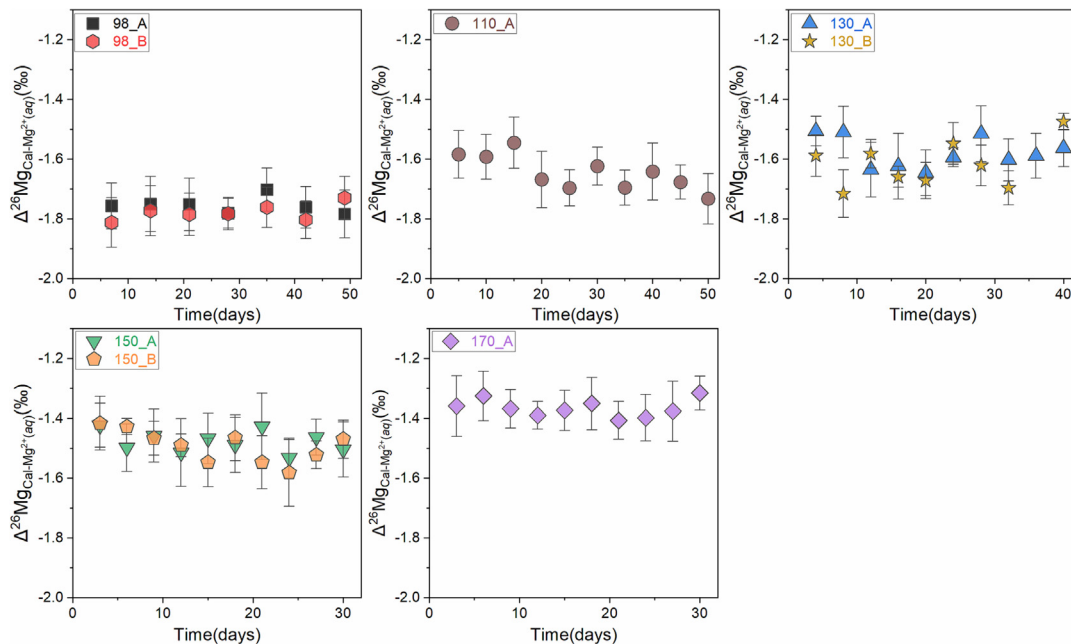
Fig. 9. The evolution of Mg isotope fractionation factors between calcite and aqueous Mg^{2+} at different experimental temperatures, details of the calculation are given in text.

$\delta^{26}Mg$ value of the aqueous solution can be expressed using the following equations:

$$\delta^{26}Mg_{soln} = (1 - f)^{\alpha-1}(1000 + \delta^{26}Mg_{soln,i}) - 1000 \quad (Rayleigh) \tag{8}$$

$$\delta^{26}Mg_{soln} = \delta^{26}Mg_{soln,i} - 1000 \times f \times \ln\alpha \quad (Batch \ equilibrium) \tag{9}$$

where f represents the proportion of total Mg that had been incorporated into calcite, α refers to the Mg isotope fractionation factor between calcite and aqueous solution, and $\delta^{26}Mg_{soln,i}$ stands for the initial isotopic composition of the solution.

As shown in Fig. 10A, Rayleigh and batch equilibrium models are similar at low extents of reaction, but diverge as f increases, especially as the reaction nears completion. With increasing f, the Rayleigh process would produce more negative apparent $\Delta^{26}Mg$ values than the batch equilibrium process (Fig. 10A). In other words, to obtain the same apparent $\Delta^{26}Mg$ values for the same f value, the batch equilibrium model requires a smaller fractionation factor, as illustrated by the data of Experiment 130_A (Fig. 10B-1, 2). The Origin@ software was used to obtain Mg isotope fractionation factors by fitting the f values and $\Delta^{26}Mg_{cal-Mg^{2+}(aq)}$ into both models (more details in supplementary material), where fractionation factors ranged from −1.78 ‰ to −1.36 ‰ for the batch equilibrium model, and −1.56 ‰ to −1.12 ‰ for the Rayleigh model (Table 3). Despite the difference in obtained fractionation
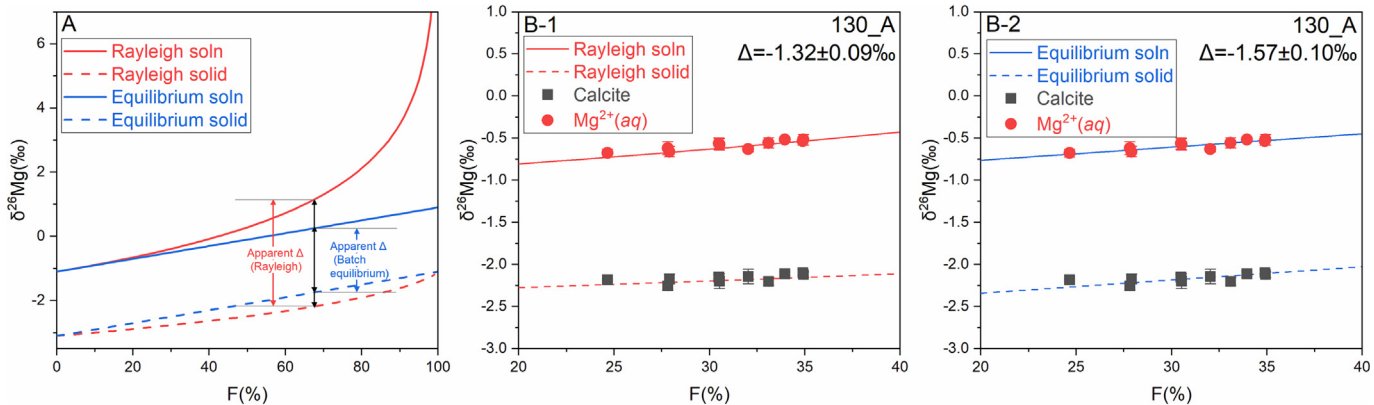
Fig. 10. (A) Theoretical evolutionary curves of Mg isotope compositions of bulk solid and aqueous phases, assuming the same Mg fractionation factor, but different models. Batch equilibrium model assumes adequate isotope exchange between solid and aqueous solutions at any stage, but Rayleigh model assumes no isotope exchange between solid and aqueous solutions after precipitation. Note the significant difference between the apparent/bulk Mg isotope fractionation factors predicted by the two models when F is large (i.e., >30 %); (B) Plot of measured Mg isotope data for Experiment 130_A in the plot of δ^{26}Mg versus F that are fitted by different models. Plot B-1 is fitted using a Rayleigh model, whereas plot B-2 is fitted using a batch equilibrium model, the two models yielded significantly different Mg isotope fractionation factors.

factors, both models can fit the experimental data well (Fig. 10B-1, 2 and Appendix Fig. S5, S6).

4.4. Temperature-dependent magnesium isotope fractionation

Stable isotope fractionation theory predicts that the equilibrium isotope fractionation factors should be dependent on temperatures (Bigeleisen and Mayer, 1947; Urey, 1947). Several experimental studies have observed such a relation between Mg isotope fractionation factors and temperature for carbonate minerals (calcite by Li et al., 2012; magnesite by Pearce et al., 2012; aragonite by Wang et al., 2013; dolomite by Li et al., 2015). Linear regression of $\Delta^{26}Mg_{cal-Mg^{2+}(aq)}$ versus $10^6/T^2$ relations (Fig. 11) produce the following equations using the isotopic fractionation factors inferred by Rayleigh or batch equilibrium processes (see above):

$$\Delta^{26}Mg_{cal-Mg^{2+}(aq)} = (-0.18 \pm 0.01) \times 10^6/T^2 - (0.22 \pm 0.06) \quad (Rayleigh) \tag{10}$$

$$\Delta^{26}Mg_{cal-Mg^{2+}(aq)} = (-0.17 \pm 0.01) \times 10^6/T^2 - (0.52 \pm 0.08) \quad (Batch \ equilibrium) \tag{11}$$

The excellent linear relationship in both plots is consistent with the theory of equilibrium isotope fractionation that fractionation factors as approximately a linear function of $1/T^2$, particularly at higher temperatures (O'Neil, 1986; Schauble, 2004; Young et al., 2015).

Table 3
The obtained Mg isotope fractionation between calcite and free Mg-aquo ions using Rayleigh and batch equilibrium models.

Experimental ID	Temperatures (°C)	Rayleigh		batch equilibrium	
		Δ^{26}Mg (‰)	2SD[1]	Δ^{26}Mg (‰)	2SD[1]
98_A	98	−1.54	0.06	−1.76	0.05
110_A	110	−1.41	0.09	−1.64	0.12
130_A	130	−1.32	0.09	−1.57	0.10
150_A	150	−1.23	0.05	−1.47	0.07
170_A	170	−1.12	0.06	−1.36	0.06
98_B	98	−1.56	0.08	−1.78	0.05
130_B	130	−1.36	0.15	−1.61	0.16
150_B	150	−1.24	0.07	−1.48	0.10

1. 2-standard deviations given by the Origin® software.

Kinetic isotope effects are commonly involved during the precipitation of carbonate for various isotope systems (e.g., Kim and O'Neil, 1997; Zhou and Zheng, 2002; Lemarchand et al., 2004; Tang et al., 2008a; AlKhatib and Eisenhauer, 2017; Guo et al., 2019), and Mg isotope fractionation may be correlated with calcite growth rate (Immenhauser et al., 2010; Mavromatis et al., 2013), perhaps reflecting kinetic issues during dehydration of Mg^{2+} aquo ions. One of the advantages of performing experiments at elevated temperatures, as in this study, is the likelihood that the water exchange of Mg^{2+} aquo ions is rapid (Bleuzen et al., 1997; Schwierz, 2020), which should reduce the kinetic effects associated with dehydration of Mg^{2+} aquo ions (Immenhauser et al., 2010; Saenger and Wang, 2014).

A key issue related to kinetic isotope effects during the precipitation of calcite is saturation state, where homogeneous precipitation experiments have required very high supersaturation states. For carbonate ion, the formation of calcite through the dissolution of aragonite will supply CO_3^{2-} via:

$$CaCO_{3(aragonite)} \rightleftharpoons Ca^{2+} + CO_3^{2-} \rightleftharpoons CaCO_{3(calcite)} \tag{12}$$

and we posit that the presence of aragonite crystals could reduce the activation energy for calcite precipitation by promoting heterogeneous nucleation (Bischoff and Fyfe, 1968). This in turn suggests that the saturation state (Ω) of calcite during the aragonite-to-calcite conversion experiment was essentially equal to the difference in the solubility products between calcite ($K_{sp,calcite}$) and aragonite ($K_{sp,aragonite}$):

$$\Omega_{calcite} = logK_{sp, aragonite} - logK_{sp, calcite} \tag{13}$$

The saturation state of calcite (<0.15) is low at high temperatures (Plummer and Busenberg, 1982) (Appendix Fig. S7), leading to the low precipitation rate of calcite (Mucci and Morse, 1983) and preventing the formation of amorphous calcium carbonate (Brečević and Nielsen, 1989). We suggest, therefore, that aragonite-to-calcite conversion is likely to produce less kinetic isotope effects than homogeneous precipitation at equivalent temperatures. Combining 1) the linear correlation between $\Delta^{26}Mg_{cal-Mg^{2+}(aq)}$ and $10^6/T^2$, 2) the elevated reaction temperatures that reduce the kinetic effects of Mg^{2+} dehydration, and 3) the low Ω and slow precipitation of calcite, we argue that the Mg isotope fractionation factors for calcite obtained in our experimental study will closely approach isotopic equilibrium. This line of reasoning is similar to that of Harrison et al. (2021), who reported that
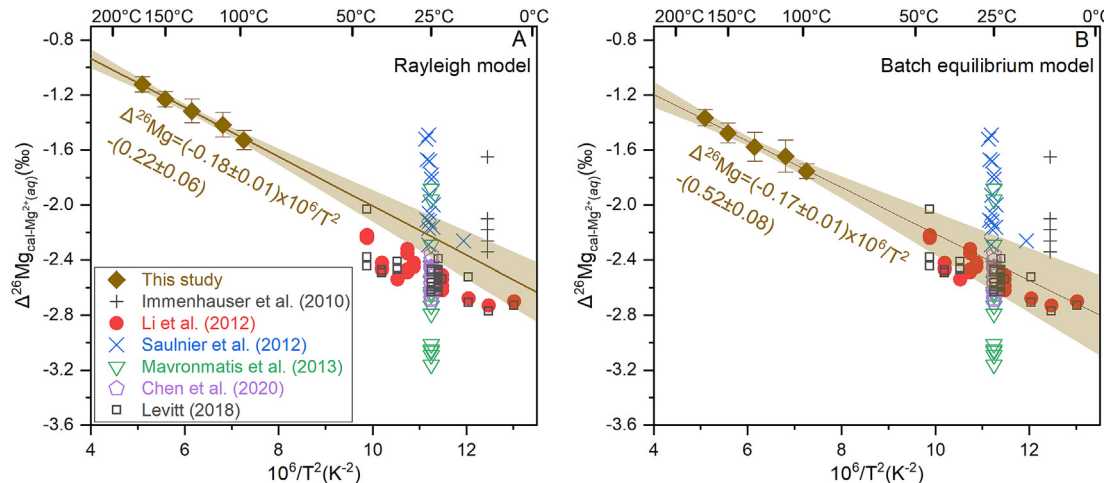
Fig. 11. Compilation plot of $\Delta^{26}Mg_{cal-Mg2+(aq)}$ versus $1/T^2$ obtained in this study and in literature. (A) The $\Delta^{26}Mg_{cal-Mg2+(aq)}$ are calculated based on Rayleigh model fitting of the experimental data, and a linear regression of the data points were made using Origin software, the shaded area represent an envelope of 95% confidence level. (B) The $\Delta^{26}Mg_{cal-Mg2+(aq)}$ are calculated based on fitting of batch equilibrium model on the experimental data, legends are the same with plot A.

equilibrium Mg isotope fractionation can be achieved between solution and dypingite when it formed by transformation of the nesquehonite.

4.5. Comparison with other experimental studies

Previous experimental studies of Mg isotope fractionation during calcite formation have tended to focus on relatively low temperatures that are analogous to natural systems (Immenhauser et al., 2010; Li et al., 2012; Saulnier et al., 2012; Mavromatis et al., 2013; Chen et al., 2020). When extrapolating equations (10) and (11) to low temperatures, the $\Delta^{26}Mg_{cal-Mg^{2+}(aq)}$ values are significantly lower than most determinations by Immenhauser et al. (2010) and Saulnier et al. (2012) (Fig. 11), suggesting that kinetic effects controlled Mg isotope fractionation dominated these studies, although the lowest values obtained by these two studies could be included in the Rayleigh trend determined here. In contrast, the results obtained here using a batch equilibrium model match quite well with those of Li et al. (2012), Levitt (2018) and Chen et al. (2020), who have reported the attainment of equilibrium Mg isotope fractionation for calcite at lower temperatures (Li et al., 2012; Levitt, 2018; Chen et al., 2020) (Fig. 11B). Using our results that were fitted to a Rayleigh model produce a trend that is significantly higher in the $\Delta^{26}Mg_{cal-Mg^{2+}(aq)}$ than those reported in previous studies (Fig. 11A). Therefore, we suggest that the batch equilibrium model (thus equation (10)) may be more appropriate to describe the Mg isotope fractionation behavior during the aragonite-to-calcite conversion experiments at hydrothermal conditions.

Using Equation (11), the equilibrium Mg isotope fractionation factor between calcite and aqueous Mg^{2+} is calculated to be −2.42 ± 0.20 ‰ at 25 °C. This $\Delta^{26}Mg_{cal-soln}$ value is consistent, within error, with those reported by Li et al. (2012), Levitt (2018), and Chen et al. (2020), but significantly higher than that proposed by Mavromatis et al. (2013). $\Delta^{26}Mg_{cal-soln}$ values in Mavromatis et al. (2013) were not only correlated with growth rate but also to the Mg content in the precipitated calcite (Appendix Fig. S8A). This correlation remains after removing the data controlled by kinetic effects (with $\Delta^{26}Mg_{cal-soln}$ values < −2.5 ‰, Appendix Fig. S8B). This might indicate that the Mg concentration in calcite may have an impact on the equilibrium Mg isotope fractionation factor, due to the lower Mg contents in calcite resulting in the longer Mg-O bond length (Wang et al., 2017). In addition, Chen

et al. (2020) noted that there was a positive correlation between the ionic strength of fluids and the measured $\Delta^{26}Mg_{cal-soln}$ in the study of Mavromatis et al. (2013), although the causal link between the two is not clear. Another possible explanation for the lower $\Delta^{26}Mg_{cal-soln}$ values may be related to the formation and transformation of amorphous carbonates (AC) during experiments. Mavromatis et al. (2017b) and Liu et al. (2022) have reported highly negative Mg isotope fractionation between carbonate minerals and solution during the AC transformation process.

4.6. Comparison with theoretical calculations

Besides experimental studies, theoretical calculations are applied to predict the equilibrium Mg isotope fractionation factors (Rustad et al., 2010; Pinilla et al., 2015; Gao et al., 2018; Wang et al., 2019; Son et al., 2020). The theoretical calculation results show the same direction of Mg isotope fractionation between calcite and solution as our experimental observations. Our experimental results, however, produce significantly less negative Mg isotope fractionation factors (Fig. 12A). It is important to note that there is a large discrepancy in predicted Mg isotope fractionation factors among theoretical studies (Fig. 12A), in part reflecting differences in calculation methods. For example, Rustad et al. (2010) obtained the equilibrium $\Delta^{26}Mg_{cal-soln}$ factors of −3.63 ‰ and −5.33 ‰ by applying the BP86 and B3LYP functionals of *ab initio* calculations, respectively at 273 K. In addition, Pinilla et al. (2015) and Gao et al. (2018) took different approaches to build the Mg aquo structure and obtained different fractionation factors than those obtained by Rustad et al. (2010), and this has been ascribed to solvation effects (Gao et al., 2018). Moreover, Wang et al. (2019) found that higher Mg contents in calcite produced a higher Mg isotope fractionation factor between calcite and solutions. It highlights the difficulties in reconciling the discrepancy between theoretical calculations and experimental data, including (1) choosing suitable functionals to solve the Schrödinger equations, (2) building the proper Mg aquo structure, (3) constructing the calcite clusters by considering the Mg concentration effects.

Wang et al. (2019) applied first-principles molecular dynamics (FPMD) simulations for the Mg aquo ion and reported calculated $\Delta^{26}Mg_{dolo-soln}$ values that are consistent with the experimentally determined $\Delta^{26}Mg_{dolo-soln}$ by Li et al. (2015). This agreement is promising in that it suggests modeling Mg in dolomite may be rel-
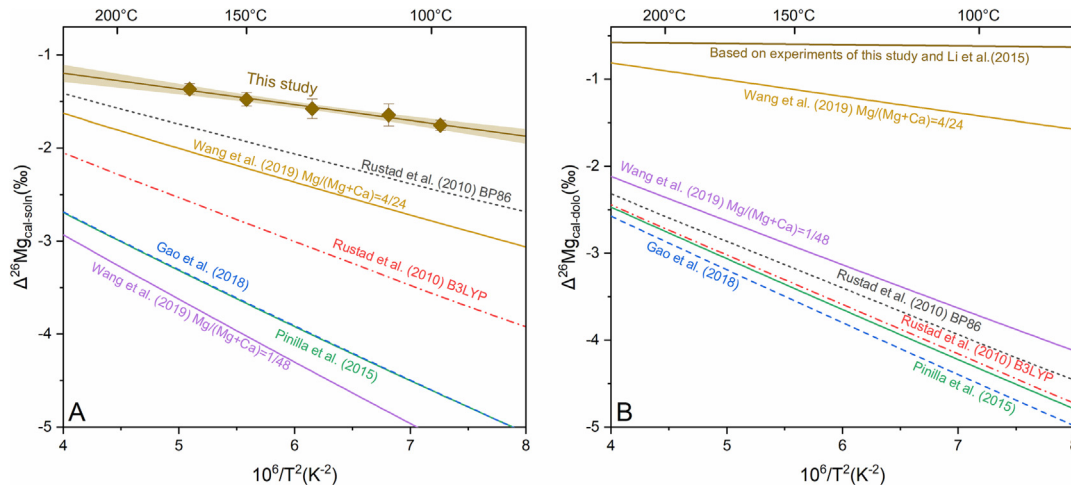
Fig. 12. (A) Comparison of the theoretical predicted $\Delta^{26}Mg_{cal\text{-}soln}$–temperature fractionation function with the experimentally calibrated data in this study (assuming batch equilibrium model). (B) Comparison of the Mg isotope fractionation factors between calcite and dolomite ($\Delta^{26}Mg_{cal\text{-}dolo}$), which is derived by the difference between $\Delta^{26}Mg_{cal\text{-}Mg2+(aq)}$ in this study and $\Delta^{26}Mg_{dolo\text{-}soln}$ from Li et al. (2015), with theoretical calculation results.

atively straightforward. The Mg isotope fractionation factor between calcite and aqueous Mg calculated by Wang et al. (2019), however, is still significantly different from those produced by our experimental data. On the other hand, combing our results with the equilibrium Mg isotope fractionation factor between dolomite and solution ($\Delta^{26}Mg_{dolo\text{-}soln}$) calibrated by Li et al. (2015), a small $\Delta^{26}Mg_{cal\text{-}dolo}$ factor is experimentally constrained (Fig. 12B). In contrast, theoretical calculation studies predicted much greater Mg isotope fractionation between calcite and dolomite (Fig. 12B), which indicates that these theoretical studies may overestimate the difference in bonds on Mg (i.e., Mg-O bond length) between calcite and dolomite.

In the previous theoretical studies, Mg atoms are assumed to be homogeneously distributed in modeled Mg-calcite lattice (cells) (Rustad et al., 2010; Pinilla et al., 2015; Gao et al., 2018; Wang et al., 2019). However, Lammers and Mitnick (2019) argued that low Mg-calcite is a non-ideal solid solution, thus the Mg substitution in natural calcite could be highly heterogeneous. This viewpoint is consistent with a number of TEM and XAF observations, which demonstrated that Mg is accommodated in domains with dolomite or other Mg-carbonate structures in calcite crystals on an nm-scale (e.g., Reksten, 1990; Wenk et al., 1991; Tsipursky and Buseck, 1993; Finch and Allison, 2007; Branson et al., 2013). It can also explain why the experimentally determined $\Delta^{26}Mg_{cal\text{-}dolo}$ (based on this study and Li et al., 2015) is small (Fig. 12B). In addition, during the growth of calcite, the incorporation of Mg leads to excess lattice strain energy due to the mismatch between Mg^{2+} and Ca^{2+} (Sethmann et al., 2010; Xu et al., 2013, 2016), which could result in plastic deformation in the calcite lattice (Hong et al., 2016). A previous study has shown that the lattice distortion may significantly affect isotope partitioning in addition to bond vibrations (Kieffer, 1982). As a consequence, simplification of the Mg occurrence in carbonate lattice settings in *ab initio* studies can lead to large inaccuracies in calculated reduced partition functions ratios (β factors) for Mg isotopes (Son et al., 2020). Therefore, we suggest that the difference in Mg distribution in the theoretically constructed Mg-calcite cluster and natural calcite as well as the strain lattice energy in Mg-calcite contributed to the difference in Mg isotope fractionation between experiments and theoretical calculations. Future theoretical studies might take the Mg-rich domain and the lattice distortion into consideration to better estimate the β factors of Mg isotopes in calcite.

4.7. Implications and potential applications

The results of this study demonstrate that Mg isotope fractionation between calcite and aqueous solutions can be achieved during aragonite-to-calcite conversion, a common process during carbonate diagenesis (Carlson, 1983), and that the relatively slow calcite formation rates associated with this process may produce isotopic fractionations that can be taken as equilibrium values. Therefore, the Mg isotopic composition of this type of calcite has the potential to reconstruct the Mg isotopic composition of fluids and environmental information during its formation. It should be noted that a recent study by He et al. (2020) proposed that the "water film" that forms during aragonite-to-calcite conversion is likely the key aspect that determines the Mg isotopic composition of calcite. This in turn indicates that the ratio of Mg contents between the surrounding fluids and aragonite would play a role in determining the Mg isotope signature of diagenetic products. Calcite of aragonite origin would record the Mg isotope composition of Mg-rich fluids such as seawater, but not the Mg-poor fluids such as meteoric water. Moreover, it should be noted that the aragonite-to-calcite conversion can take place during burial diagenesis, where fluid-rock reaction would lead to alteration of fluid compositions, which are unlikely to reflect seawater. As a consequence, calcite may no longer record the Mg isotopic information of seawater.

Marine biogenic calcites show a large variation of Mg isotopic composition (Saenger and Wang, 2014 and references therein), corresponding to apparent $\Delta^{26}Mg_{cal\text{-}soln}$ factors ranging from -4.75 ‰ to -0.22 ‰. For those with higher $\Delta^{26}Mg_{cal\text{-}soln}$ than the equilibrium fractionation factors (Hippler et al., 2009; Ra et al., 2010a, b; Müller et al., 2011; Wombacher et al., 2011; Yoshimura et al., 2011), kinetic isotope effects should play an important role (Mavromatis et al., 2013). In contrast, some marine organisms, like planktonic foraminifera and bivalves, appear to have formed with more negative Mg isotope fractionation between calcite and seawater than that is seen in experiments (Pogge von Strandmann, 2008; Hippler et al., 2009; Wombacher et al., 2011). These observations indicate that the biomineralization process or "vital effects" may significantly influence Mg isotope fractionation. The exact mechanisms by which this occurs, however, are still poorly understood (Immenhauser et al., 2016). Several hypotheses have been proposed to explain these phenomena, including prefer-

ential uptake of lighter Mg isotopes through cell membranes (Hippler et al., 2009), Mg isotope fractionation associated with the formation of Mg-biomolecule ligands in cell body fluids (Wombacher et al., 2011), and the formation of AC (Saenger and Wang, 2014; Mavromatis et al., 2017b). Recognition of "vital effects" are, of course, only possible in the context of establishing equilibrium isotope fractionation functions.

Our results are most directly applicable to temperature conditions that overlap the experiments, such as calcite precipitation related to the burial and hydrothermal process. Calcite formation during burial diagenesis is, for example, one of the most important cementation minerals controlling water or hydrocarbon reservoir quality (e.g., Heydari, 1997; Salem et al., 2000; Dutton, 2008; Cai et al., 2014; Wang et al., 2020), and hydrothermal calcite can host significant base and metal ore deposits (e.g., Yang and Zhou, 2001; Hedenquist et al., 2005; Hu et al., 2008; Shu et al., 2013; Zhou et al., 2013). The geochemical characteristics of these two types of calcite have been applied to trace their formation mechanism (e.g., Bjørkum and Walderhaug, 1990; Dravis, 1996; Molenaar and Zijlstra, 1997; Xiong et al., 2016), as well as ore-forming process (e.g., Brown et al., 1985; Large et al., 2001; Torres-Ruiz, 2006; Vaughan et al., 2016; Du et al., 2017). In addition, Walter et al. (2015) pointed out that the Mg isotope composition of hydrothermal carbonates, including calcite and dolomite, could be a useful tracer of hydrothermal fluids. Recently, Xie et al. (2022) applied Mg isotopes of hydrothermal carbonates in Carlin-type gold deposits to constrain the nature of ore-forming fluids. Our study provided a rigorously constrained function of equilibrium Mg isotope fractionation factors between calcite and fluids that can be applied to elevated temperatures, thus enabling more confident applications of Mg isotopes to calcite of hydrothermal and deep burial origin for various geological problems.

5. Conclusion

The Mg isotope fractionation between calcite and aqueous solution has been investigated at hydrothermal conditions (98 °C to 170 °C) by conducting aragonite to calcite conversion experiments. The apparent Mg isotope fractionation factors between bulk calcite and aqueous solutions ($\Delta^{26}Mg_{cal-soln}$) range from ca.-1.84 ‰ at 98 °C to −1.35 ‰ at 170 °C and are positively correlated with reaction temperature. Besides temperature, the presence of oxalate is found to influence the $\Delta^{26}Mg_{cal-soln}$ by forming the Mg-oxalate complex. Although both Rayleigh and batch equilibrium models could fit the experimental data well, we proposed that Mg isotope fractionation during the experiments followed a batch equilibrium model. The equilibrium Mg isotope fractionation factor between calcite and aqueous Mg^{2+} can be expressed as;

$$\Delta^{26}Mg_{cal-Mg^{2+}(aq)} = (-0.17 \pm 0.01) \times 10^6/T^2 - (0.52 \pm 0.08)$$

where T is in Kelvin.

Our results provide new insights for understanding Mg isotope behavior associated with calcite precipitation. For example, the equation of equilibrium Mg isotope fractionation sets a baseline for further investigation of the "vital effect" on the Mg isotope fractionation behavior during biomineralization. The newly calibrated Mg isotope fractionation function could also be applied to study the hydrothermal thermal and burial process at elevated temperatures by calcite records, which opens a window for new applications of Mg isotope hydrothermal geochemistry.

Data availability

Data will be made available on request.

Declaration of Competing Interest

The authors declare that they have no known competing financial interests or personal relationships that could have appeared to influence the work reported in this paper.

Appendix A. Supplementary material

Research data is provided within the Supplementary Material. Supplementary material to this article can be found online at https://doi.org/10.1016/j.gca.2022.12.017.

References

Agrinier, P., Javoy, M., 2016. Unbiased isotope equilibrium factors from partial isotope exchange experiments in 3-exchange site systems. Geochim. Cosmochim. Acta 189, 197–213.

Ahm, A.-S.-C., Bjerrum, C.J., Blättler, C.L., Swart, P.K., Higgins, J.A., 2018. Quantifying early marine diagenesis in shallow-water carbonate sediments. Geochim. Cosmochim. Acta 236, 140–159.

Ahm, A.-S.-C., Maloof, A.C., Macdonald, F.A., Hoffman, P.F., Bjerrum, C.J., Bold, U., Rose, C.V., Strauss, J.V., Higgins, J.A., 2019. An early diagenetic deglacial origin for basal Ediacaran "cap dolostones". Earth Planet. Sci. Lett. 506, 292–307.

AlKhatib, M., Eisenhauer, A., 2017. Calcium and strontium isotope fractionation in aqueous solutions as a function of temperature and reaction rate; I. Calcite. Geochim. Cosmochim. Acta 209, 296–319.

Baker, P.A., Gieskes, J.M., Elderfield, H., 1982. Diagenesis of carbonates in deep-sea sediments; evidence from Sr/Ca ratios and interstitial dissolved Sr^{2+} data. J. Sediment. Res. 52, 71–82.

Bialik, O.M., Wang, X., Zhao, S., Waldmann, N.D., Frank, R., Li, W., 2018. Mg isotope response to dolomitization in hinterland-attached carbonate platforms: Outlook of $\delta^{26}Mg$ as a tracer of basin restriction and seawater Mg/Ca ratio. Geochim. Cosmochim. Acta 235, 189–207.

Bigeleisen, J., Mayer, M.G., 1947. Calculation of equilibrium constants for isotopic exchange reactions. J. Chem. Phys. 15, 261–267.

Bischoff, J.L., Fyfe, W.S., 1968. Catalysis, inhibition, and the calcite-aragonite problem; [Part] 1, The aragonite-calcite transformation. Am. J. Sci. 266, 65–79.

Bjørkum, P.A., Walderhaug, O., 1990. Geometrical arrangement of calcite cementation within shallow marine sandstones. Earth-Sci Rev 29, 145–161.

Bleuzen, A., Pittet, P.-A., Helm, L., Merbach, A.E., 1997. Water exchange on magnesium(II) in aqueous solution: a variable temperature and pressure 17O NMR study. Magn. Reson. Chem. 35, 765–773.

Branson, O., Redfern, S.A.T., Tyliszczak, T., Sadekov, A., Langer, G., Kimoto, K., Elderfield, H., 2013. The coordination of Mg in foraminiferal calcite. Earth Planet. Sci. Lett. 383, 134–141.

Brečević, L., Nielsen, A.E., 1989. Solubility of amorphous calcium carbonate. J. Cryst. Growth 98, 504–510.

Brown, P.E., Bowman, J.R., Kelly, W.C., 1985. Petrologic and stable isotope constraints on the source and evolution of skarn-forming fluids at Pine Creek, California. Econ. Geol. 80, 72–95.

Burton, E.A., Walter, L.M., 1991. The effects of PCO_2 and temperature on magnesium incorporation in calcite in seawater and $MgCl_2$-$CaCl_2$ solutions. Geochim. Cosmochim. Acta 55, 777–785.

Cai, C., He, W., Jiang, L., Li, K., Xiang, L., Jia, L., 2014. Petrological and geochemical constraints on porosity difference between Lower Triassic sour- and sweet-gas carbonate reservoirs in the Sichuan Basin. Mar. Pet. Geol. 56, 34–50.

Carlson, W.D., 1983. The polymorphs of $CaCO_3$ and the aragonite-calcite transformation. Rev. Mineral. Geochem. 11, 191–225.

Chanda, P., Fantle, M.S., 2017. Quantifying the effect of diagenetic recrystallization on the Mg isotopic composition of marine carbonates. Geochim. Cosmochim. Acta 204, 219–239.

Chang, V.T.C., Williams, R.J.P., Makishima, A., Belshawl, N.S., O'Nions, R.K., 2004. Mg and Ca isotope fractionation during $CaCO_3$ biomineralisation. Biochem. Biophys. Res. Commun. 323, 79–85.

Chen, X.-Y., Teng, F.-Z., Sanchez, W.R., Romanek, C.S., Sanchez-Navas, A., Sánchez-Román, M., 2020. Experimental constraints on magnesium isotope fractionation

during abiogenic calcite precipitation at room temperature. Geochim. Cosmochim. Acta 281, 102–117.

Cole, D.R., Ripley, E.M., 1999. Oxygen isotope fractionation between chlorite and water from 170 to 350°C: a preliminary assessment based on partial exchange and fluid/rock experiments. Geochim. Cosmochim. Acta 63, 449–457.

Crockford, P.W., Kunzmann, M., Blättler, C.L., Kalderon-Asael, B., Murphy, J.G., Ahm, A.-S., Sharoni, S., Halverson, G.P., Planavsky, N.J., Halevy, I., Higgins, J.A., 2020. Reconstructing Neoproterozoic seawater chemistry from early diagenetic dolomite. Geology 49, 442–446.

Day, C.C., Henderson, G.M., 2013. Controls on trace-element partitioning in cave-analogue calcite. Geochim. Cosmochim. Acta 120, 612–627.

de Villiers, S., Greaves, M., Elderfield, H., 2002. An intensity ratio calibration method for the accurate determination of Mg/Ca and Sr/Ca of marine carbonates by ICP-AES. Geochem. Geophys. Geosyst., 3

Dietzel, M., Usdowski, E., 1996. Coprecipitation of Ni^{2+}, Co^{2+}, and Mn^{2+} with galena and covellite, and of Sr^{2+} with calcite during crystallization via diffusion of H_2S and CO_2 through polyethylene at 20°C: Power law and Nernst law control of trace element partitioning. Chem. Geol. 131, 55–65.

Dravis, J.J., 1996. Rapidity of freshwater calcite cementation—implications for carbonate diagenesis and sequence stratigraphy. Sed. Geol. 107, 1–10.

Drysdale, R.N., Zanchetta, G., Baneschi, I., Guidi, M., Isola, I., Couchoud, I., Piccini, L., Greig, A., Wong, H., Woodhead, J.D., Regattieri, E., Corrick, E., Paul, B., Spötl, C., Denson, E., Gordon, J., Jaillet, S., Dux, F., Hellstrom, J.C., 2019. Partitioning of Mg, Sr, Ba and U into a subaqueous calcite speleothem. Geochim. Cosmochim. Acta 264, 67–91.

Du, L.-J., Li, B., Huang, Z.-L., Zhou, J.-X., Zou, G.-F., Yan, Z.-F., 2017. Carbon-oxygen isotopic geochemistry of the Yangla Cu skarn deposit, SW China: Implications for the source and evolution of hydrothermal fluids. Ore Geol. Rev. 88, 809–821.

Dutton, S.P., 2008. Calcite cement in Permian deep-water sandstones, Delaware Basin west Texas: Origin, distribution, and effect on reservoir properties. AAPG Bull. 92, 765–787.

Fantle, M.S., Barnes, B.D., Lau, K.V., 2020. The role of diagenesis in shaping the geochemistry of the marine carbonate record. Annu. Rev. Earth Planet. Sci. 48, 549–583.

Fantle, M.S., Higgins, J., 2014. The effects of diagenesis and dolomitization on Ca and Mg isotopes in marine platform carbonates: Implications for the geochemical cycles of Ca and Mg. Geochim. Cosmochim. Acta 142, 458–481.

Finch, A.A., Allison, N., 2007. Coordination of Sr and Mg in calcite and aragonite. Mineral. Mag. 71, 539–552.

Gabitov, R.I., Sadekov, A., Leinweber, A., 2014. Crystal growth rate effect on Mg/Ca and Sr/Ca partitioning between calcite and fluid: An in situ approach. Chem. Geol. 367, 70–82.

Gabitov, R.I., Sadekov, A., Dyer, J., Perez-Huerta, A., Xu, H., Migdisov, A., 2021. Sectoral and growth rate control on elemental uptake by individual calcite crystals. Chem. Geol. 585, 120589.

Gabitov, R.I., Watson, E.B., 2006. Partitioning of strontium between calcite and fluid. Geochem. Geophys. Geosyst., 7

Gao, C., Cao, X., Liu, Q., Yang, Y., Zhang, S., He, Y., Tang, M., Liu, Y., 2018. Theoretical calculation of equilibrium Mg isotope fractionations between minerals and aqueous solutions. Chem. Geol. 488, 62–75.

Gascoyne, M., 1983. Trace-element partition coefficients in the calcite-water system and their paleoclimatic significance in cave studies. J. Hydrol. 61, 213–222.

Gautier, Q., Berninger, U.-N., Schott, J., Jordan, G., 2015. Influence of organic ligands on magnesite growth: A hydrothermal atomic force microscopy study. Geochim. Cosmochim. Acta 155, 68–85.

Goetschl, K.E., Purgstaller, B., Dietzel, M., Mavromatis, V., 2019. Effect of sulfate on magnesium incorporation in low-magnesium calcite. Geochim. Cosmochim. Acta 265, 505–519.

Gothmann, A.M., Stolarski, J., Adkins, J.F., Higgins, J.A., 2017. A Cenozoic record of seawater Mg isotopes in well-preserved fossil corals. Geology 45, 1039–1042.

Guo, Y., Deng, W., Wei, G., 2019. Kinetic effects during the experimental transition of aragonite to calcite in aqueous solution: Insights from clumped and oxygen isotope signatures. Geochim. Cosmochim. Acta 248, 210–230.

Harrison, A.L., Bénézeth, P., Schott, J., Oelkers, E.H., Mavromatis, V., 2021. Magnesium and carbon isotope fractionation during hydrated Mg-carbonate mineral phase transformations. Geochim. Cosmochim. Acta 293, 507–524.

Hartley, G., Mucci, A., 1996. The influence of PCO₂ on the partitioning of magnesium in calcite overgrowths precipitated from artificial seawater at 25° and 1 atm total pressure. Geochim. Cosmochim. Acta 60, 315–324.

He, R., Ning, M., Huang, K., Ma, H., Shen, B., 2020. Mg isotopic systematics during early diagenetic aragonite-calcite transition: Insights from the Key Largo Limestone. Chem. Geol. 558, 119876.

Hedenquist, J.W., Thompson, J.F.H., Goldfarb, R.J., Richards, J.P., 2005. One Hundredth Anniversary Volume. Society of Economic Geologists.

Heydari, E., 1997. The role of burial diagenesis in hydrocarbon destruction and H_2S accumulation, upper Jurassic Smackover Formation, Black Creek Field, Mississippi. AAPG Bull. Am. Assoc. Pet. Geol. 81, 26–45.

Higgins, J.A., Schrag, D.P., 2012. Records of Neogene seawater chemistry and diagenesis in deep-sea carbonate sediments and pore fluids. Earth Planet. Sci. Lett. 357, 386–396.

Hippler, D., Buhl, D., Witbaard, R., Richter, D.K., Immenhauser, A., 2009. Towards a better understanding of magnesium-isotope ratios from marine skeletal carbonates. Geochim. Cosmochim. Acta 73, 6134–6146.

Holland, H.D., Holland, H.J., Munoz, J.L., 1964. The coprecipitation of cations with CaCO3—II. The coprecipitation of Sr+2 with calcite between 90° and 100°C. Geochim. Cosmochim. Acta 28, 1287–1301.

Hong, M., Xu, J., Teng, H.H., 2016. Evolution of calcite growth morphology in the presence of magnesium: Implications for the dolomite problem. Geochim. Cosmochim. Acta 172, 55–64.

Howson, M.R., Pethybridge, A.D., House, W.A., 1987. Synthesis and distribution coefficient of low-magnesium calcites. Chem. Geol. 64, 79–87.

Hu, R.Z., Bi, X.W., Zhou, M.F., Peng, J.T., Su, W.C., Liu, S., Qi, H.W., 2008. Uranium metallogenesis in South China and its relationship to crustal extension during the Cretaceous to Tertiary. Econ. Geol. 103, 583–598.

Hu, Z., Hu, W., Wang, X., Lu, Y., Wang, L., Liao, Z., Li, W., 2017. Resetting of Mg isotopes between calcite and dolomite during burial metamorphism: Outlook of Mg isotopes as geothermometer and seawater proxy. Geochim. Cosmochim. Acta 208, 24–40.

Hu, Z., Bialik, O.M., Hohl, S.V., Xia, Z., Waldmann, N.D., Liu, C., Li, W., 2021a. Response of Mg isotopes to dolomitization during fluctuations in sea level: Constraints on the hydrological conditions of massive dolomitization systems. Sed. Geol. 420, 105922.

Hu, Z., Li, W., Zhang, H., Krainer, K., Zheng, Q.-F., Xia, Z., Hu, W., Shen, S.-Z., 2021b. Mg isotope evidence for restriction events within the Paleotethys ocean around the Permian-Triassic transition. Earth Planet. Sci. Lett. 556, 116704.

Huang, Y., Fairchild, I.J., Borsato, A., Frisia, S., Cassidy, N.J., McDermott, F., Hawkesworth, C.J., 2001. Seasonal variations in Sr, Mg and P in modern speleothems (Grotta di Ernesto, Italy). Chem. Geol. 175, 429–448.

Huang, Y., Fairchild, I.J., 2001. Partitioning of Sr^{2+} and Mg^{2+} into calcite under karst-analogue experimental conditions. Geochim. Cosmochim. Acta 65, 47–62.

Huang, K.-J., Shen, B., Lang, X.-G., Tang, W.-B., Peng, Y., Ke, S., Kaufman, A.J., Ma, H.-R., Li, F.-B., 2015. Magnesium isotopic compositions of the Mesoproterozoic dolostones: Implications for Mg isotopic systematics of marine carbonates. Geochim. Cosmochim. Acta 164, 333–351.

Humphrey, J.D., Howell, R.P., 1999. Effect of differential stress on strontium partitioning in calcite. J. Sediment. Res. 69, 208–215.

Immenhauser, A., Buhl, D., Richter, D., Niedermayr, A., Riechelmann, D., Dietzel, M., Schulte, U., 2010. Magnesium-isotope fractionation during low-Mg calcite precipitation in a limestone cave - Field study and experiments. Geochim. Cosmochim. Acta 74, 4346–4364.

Immenhauser, A., Schöne, B.R., Hoffmann, R., Niedermayr, A., 2016. Mollusc and brachiopod skeletal hard parts: Intricate archives of their marine environment. Sedimentology 63, 1–59.

Jacobson, R.L., Usdowski, H.E., 1976. Partitioning of strontium between calcite, dolomite and liquids: An experimental study under higher temperature diagenetic conditions, and a model for the prediction of mineral pairs for geothermometry. Contrib. Miner. Petrol. 59, 171–185.

Johnson, J.W., Oelkers, E.H., Helgeson, H.C., 1992. SUPCRT92: A software package for calculating the standard molal thermodynamic properties of minerals, gases, aqueous species, and reactions from 1 to 5000 bar and 0 to 1000°C. Comput. Geosci. 18, 899–947.

Katz, A., 1973. The interaction of magnesium with calcite during crystal growth at 25–90°C and one atmosphere. Geochim. Cosmochim. Acta 37, 1563–1586.

Katz, A., Sass, E., Starinsky, A., Holland, H.D., 1972. Strontium behavior in the aragonite-calcite transformation: An experimental study at 40–98°C. Geochim. Cosmochim. Acta 36, 481–496.

Kieffer, S.W., 1982. Thermodynamics and lattice vibrations of minerals: 5. Applications to phase equilibria, isotopic fractionation, and high-pressure thermodynamic properties. Rev. Geophys. 20, 827–849.

Kim, S.-T., O'Neil, J.R., 1997. Equilibrium and nonequilibrium oxygen isotope effects in synthetic carbonates. Geochim. Cosmochim. Acta 61, 3461–3475.

Kimmig, S.R., Nadeau, M.D., Swart, P.K., Holmden, C., 2021. Mg and Sr isotopic evidence for basin wide alteration of early diagenetic dolomite in the Williston Basin by ascending crustal fluids. Geochim. Cosmochim. Acta 311, 198–225.

Kontoyannis, C.G., Vagenas, N.V., 2000. Calcium carbonate phase analysis using XRD and FT-Raman spectroscopy. Analyst 125, 251–255.

Lammers, L.N., Mitnick, E.H., 2019. Magnesian calcite solid solution thermodynamics inferred from authigenic deep-sea carbonate. Geochim. Cosmochim. Acta 248, 343–355.

Land, L.S., 1998. Failure to precipitate dolomite at 25°C from dilute solution despite 1000-fold oversaturation after 32 years. Aquat. Geochem. 4, 361–368.

Large, R.R., Bull, S.W., Winefield, P.R., 2001. Carbon and Oxygen Isotope Halo in Carbonates Related to the McArthur River (HYC) Zn-Pb-Ag Deposit, North Australia: Implications for Sedimentation, Ore Genesis, and Mineral Exploration. Econ. Geol. 96, 1567–1593.

Lemarchand, D., Wasserburg, G.J., Papanastassiou, D.A., 2004. Rate-controlled calcium isotope fractionation in synthetic calcite. Geochim. Cosmochim. Acta 68, 4665–4678.

Levitt, N.P., 2018. New Views of Carbonates as a Proxy for Ancient Seawater and Paleoenvironments: ¹³C-¹⁸O Clumped Isotopes and Stable Mg Isotopes. Ph.D. thesis, University of Wisconsin-Madison, 396 pages.

Li, W., Chakraborty, S., Beard, B.L., Romanek, C.S., Johnson, C.M., 2012. Magnesium isotope fractionation during precipitation of inorganic calcite under laboratory conditions. Earth Planet. Sci. Lett. 333, 304–316.

Li, W., Beard, B.L., Johnson, C.M., 2011. Exchange and fractionation of Mg isotopes between epsomite and saturated $MgSO_4$ solution. Geochim. Cosmochim. Acta 75, 1814–1828.

Li, W., Beard, B.L., Li, C., Johnson, C.M., 2014. Magnesium isotope fractionation between brucite $[Mg(OH)_2]$ and Mg aqueous species: Implications for silicate weathering and biogeochemical processes. Earth Planet. Sci. Lett. 394, 82–93.

Li, W., Beard, B.L., Li, C., Xu, H., Johnson, C.M., 2015. Experimental calibration of Mg isotope fractionation between dolomite and aqueous solution and its geological implications. Geochim. Cosmochim. Acta 157, 164–181.

Li, W., Bialik, O.M., Wang, X., Yang, T., Hu, Z., Huang, Q., Zhao, S., Waldmann, N.D., 2019. Effects of early diagenesis on Mg isotopes in dolomite: The roles of Mn (IV)-reduction and recrystallization. Geochim. Cosmochim. Acta 250, 1–17.

Lippmann, F., 1973. Sedimentary Carbonate Minerals. Springer-Verlag, Berlin Heidelberg.

Liu, C., Wang, K., Li, W., 2022. Isotopic responses of Mg to two types of dissolution-reprecipitation processes for the growth of the double-carbonate mineral norsethite. American Mineralogist In press. doi: 10.2138/am-2022-8386.

Lorens, R.B., 1981. Sr, Cd, Mn and Co distribution coefficients in calcite as a function of calcite precipitation rate. Geochim. Cosmochim. Acta 45, 553–561.

Malone, M.J., Baker, P.A., 1999. Temperature dependence of the strontium distribution coefficient in calcite; an experimental study from 40 degrees to 200 degrees C and application to natural diagenetic calcites. J. Sediment. Res. 69, 216–223.

Mavromatis, V., Gautier, Q., Bosc, O., Schott, J., 2013. Kinetics of Mg partition and Mg stable isotope fractionation during its incorporation in calcite. Geochim. Cosmochim. Acta 114, 188–203.

Mavromatis, V., Immenhauser, A., Buhl, D., Purgstaller, B., Baldermann, A., Dietzel, M., 2017a. Effect of organic ligands on Mg partitioning and Mg isotope fractionation during low-temperature precipitation of calcite in the absence of growth rate effects. Geochim. Cosmochim. Acta 207, 139–153.

Mavromatis, V., Purgstaller, B., Dietzel, M., Buhl, D., Immenhauser, A., Schott, J., 2017b. Impact of amorphous precursor phases on magnesium isotope signatures of Mg-calcite. Earth Planet. Sci. Lett. 464, 227–236.

Molenaar, N., Zijlstra, J.J.P., 1997. Differential early diagenetic low-Mg calcite cementation and rhythmic hardground development in Campanian-Maastrichtian chalk. Sed. Geol. 109, 261–281.

Morse, J.W., Arvidson, R.S., Lüttge, A., 2007. Calcium Carbonate Formation and Dissolution. Chem. Rev. 107, 342–381.

Morse, J.W., Mackenzie, F.T., 1990. Geochemistry of Sedimentary Carbonates. Elsevier Science.

Mucci, A., 1986. Growth kinetics and composition of magnesian calcite overgrowths precipitated from seawater: Quantitative influence of orthophosphate ions. Geochim. Cosmochim. Acta 50, 2255–2265.

Mucci, A., 1987. Influence of temperature on the composition of magnesian calcite overgrowths precipitated from seawater. Geochim. Cosmochim. Acta 51, 1977–1984.

Mucci, A., Morse, J.W., 1983. The incorporation of Mg^{2+} and Sr^{2+} into calcite overgrowths: influences of growth rate and solution composition. Geochim. Cosmochim. Acta 47, 217–233.

Müller, M.N., Kısakürek, B., Buhl, D., Gutperlet, R., Kolevica, A., Riebesell, U., Stoll, H., Eisenhauer, A., 2011. Response of the coccolithophores Emiliania huxleyi and Coccolithus braarudii to changing seawater Mg^{2+} and Ca^{2+} concentrations: Mg/Ca, Sr/Ca ratios and $\delta^{44/40}Ca$, $\delta^{26/24}Mg$ of coccolith calcite. Geochim. Cosmochim. Acta 75, 2088–2102.

Nehrke, G., Reichart, G.J., Van Cappellen, P., Meile, C., Bijma, J., 2007. Dependence of calcite growth rate and Sr partitioning on solution stoichiometry: Non-Kossel crystal growth. Geochim. Cosmochim. Acta 71, 2240–2249.

Ning, M., Lang, X., Huang, K., Li, C., Huang, T., Yuan, H., Xing, C., Yang, R., Shen, B., 2020. Towards understanding the origin of massive dolostones. Earth Planet. Sci. Lett. 545, 116403.

O'Neil, J.R., 1986. Theoretical and experimental aspects of isotopic fractionation. Rev. Mineral. Geochem. 16, 1–40.

Oomori, T., Kaneshima, H., Maezato, Y., Kitano, Y., 1987. Distribution coefficient of Mg^{2+} ions between calcite and solution at 10–50°C. Mar. Chem. 20, 327–336.

Pearce, C.R., Saldi, G.D., Schott, J., Oelkers, E.H., 2012. Isotopic fractionation during congruent dissolution, precipitation and at equilibrium: Evidence from Mg isotopes. Geochim. Cosmochim. Acta 92, 170–183.

Pederson, C.L., Weiss, L., Mavromatis, V., Rollion-Bard, C., Dietzel, M., Neuser, R., Immenhauser, A., 2019. Significance of fluid chemistry throughout diagenesis of aragonitic Porites corals – An experimental approach. Depositional Rec. 5, 592–612.

Pederson, C.L., Mavromatis, V., Dietzel, M., Rollion-Bard, C., Breitenbach, S.F.M., Yu, D., Nehrke, G., Immenhauser, A., 2020. Variation in the diagenetic response of aragonite archives to hydrothermal alteration. Sed. Geol. 406, 105716.

Pingitore, N.E., Eastman, M.P., 1986. The coprecipitation of Sr^{2+} with calcite at 25°C and 1 atm. Geochim. Cosmochim. Acta 50, 2195–2203.

Pinilla, C., Blanchard, M., Balan, E., Natarajan, S.K., Vuilleumier, R., Mauri, F., 2015. Equilibrium magnesium isotope fractionation between aqueous Mg^{2+} and carbonate minerals: Insights from path integral molecular dynamics. Geochim. Cosmochim. Acta 167, 313–314.

Planchon, F., Poulain, C., Langlet, D., Paulet, Y.-M., André, L., 2013. Mg-isotopic fractionation in the manila clam (Ruditapes philippinarum): New insights into Mg incorporation pathway and calcification process of bivalves. Geochim. Cosmochim. Acta 121, 374–397.

Plummer, L.N., Busenberg, E., 1982. The solubilities of calcite, aragonite and vaterite in CO_2-H_2O solutionss between 0 and 90°C and evalution of the aqueous model for the system $CaCO_3$-CO_2-H_2O. Geochim. Cosmochim. Acta 46, 1011–1040.

Pogge von Strandmann, P.A.E., 2008. Precise magnesium isotope measurements in core top planktic and benthic foraminifera. Geochem. Geophys., Geosyst. 9

Pogge von Strandmann, P.A.E., Forshaw, J., Schmidt, D.N., 2014. Modern and Cenozoic records of seawater magnesium from foraminiferal Mg isotopes. Biogeosciences 11, 5155–5168.

Prapaipong, P., Shock, E.L., Koretsky, C.M., 1999. Metal-organic complexes in geochemical processes: temperature dependence of the standard thermodynamic properties of aqueous complexes between metal cations and dicarboxylate ligands. Geochim. Cosmochim. Acta 63, 2547–2577.

Ra, K., Kitagawa, H., Shiraiwa, Y., 2010a. Mg isotopes and Mg/Ca values of coccoliths from cultured specimens of the species Emiliania huxleyi and Gephyrocapsa oceanica. Mar. Micropaleontol. 77, 119–124.

Ra, K., Kitagawa, H., Shiraiwa, Y., 2010b. Mg isotopes in chlorophyll-a and coccoliths of cultured coccolithophores (Emiliania huxleyi) by MC-ICP-MS. Mar. Chem. 122, 130–137.

Reksten, K., 1990. Superstructures in calcite. Am. Mineral. 75, 807–812.

Rustad, J.R., Casey, W.H., Yin, Q.-Z., Bylaska, E.J., Felmy, A.R., Bogatko, S.A., Jackson, V.E., Dixon, D.A., 2010. Isotopic fractionation of $Mg^{2+}(aq)$, $Ca^{2+}(aq)$, and $Fe^{2+}(aq)$ with carbonate minerals. Geochim. Cosmochim. Acta 74, 6301–6323.

Saccoccia, P.J., Seewald, J.S., Shanks, W.C., 1998. Hydrogen and Oxygen Isotope Fractionation Between Brucite and Aqueous NaCl Solutions from 250 to 450°C. Geochim. Cosmochim. Acta 62, 485–492.

Saccoccia, P.J., Seewald, J.S., Shanks, W.C., 2015. Oxygen isotope fractionation in the portlandite–water and brucite–water systems from 125 to 450°C, 50MPa. Geochim. Cosmochim. Acta 169, 137–151.

Saenger, C., Wang, Z., 2014. Magnesium isotope fractionation in biogenic and abiogenic carbonates: implications for paleoenvironmental proxies. Quat. Sci. Rev. 90, 1–21.

Salem, A.M., Morad, S., Mato, L.F., Al-Aasm, I.S., 2000. Diagenesis and reservoir-quality evolution of fluvial sandstones during progressive burial and uplift: Evidence from the Upper Jurassic Boipeba Member, Reconcavo basin, northeastern Brazil. AAPG Bull. 84, 1015–1040.

Saulnier, S., Rollion-Bard, C., Vigier, N., Chaussidon, M., 2012. Mg isotope fractionation during calcite precipitation: An experimental study. Geochim. Cosmochim. Acta 91, 75–91.

Schauble, E.A., 2004. Applying stable isotope fractionation theory to new systems. Geochem. Non-Traditional Stable Isotopes 55, 65–111.

Schott, J., Mavromatis, V., Fujii, T., Pearce, C.R., Oelkers, E.H., 2016. The control of carbonate mineral Mg isotope composition by aqueous speciation: Theoretical and experimental modeling. Chem. Geol. 445, 120–134.

Schwierz, N., 2020. Kinetic pathways of water exchange in the first hydration shell of magnesium. J. Chem. Phys. 152, 224106.

Sethmann, I., Wang, J., Becker, U., Putnis, A., 2010. Strain-Induced Segmentation of Magnesian Calcite Thin Films Growing on a Calcite Substrate. Cryst. Growth Des. 10, 4319–4326.

Shahar, A., Elardo, S.M., Macris, C.A., 2017. Equilibrium Fractionation of Non-traditional Stable Isotopes: an Experimental Perspective. Rev. Mineral. Geochem. 82, 65–83.

Shannon, R.D., 1976. Revised effective ionic-radii and systematic studies of interatomic distances in halides and chalcogenides. Acta Crystallogr. A 32, 751–767.

Shu, Q.H., Lai, Y., Sun, Y., Wang, C., Meng, S., 2013. Ore Genesis and Hydrothermal Evolution of the Baiyinnuo'er Zinc-Lead Skarn Deposit, Northeast China: Evidence from Isotopes (S, Pb) and Fluid Inclusions. Econ. Geol. 108, 835–860.

Son, S., Li, W., Lee, J.-Y., Kwon, K.D., 2020. On the coordination of Mg^{2+} in aragonite: Ab-initio absorption spectroscopy and isotope fractionation study. Geochim. Cosmochim. Acta 286, 324–335.

Stamm, F.M., Méheut, M., Zambardi, T., Chmeleff, J., Schott, J., Oelkers, E.H., 2022. Determination of the equilibrium magnesium isotope fractionation factors between brucite and aqueous inorganic and organic species. Geochim. Cosmochim. Acta 336, 33–49.

Stoessell, R.K., Klimentidis, R.E., Prezbindowski, D.R., 1987. Dedolomitization in Na Ca Cl brines from 100° to 200°C at 300 bars. Geochim. Cosmochim. Acta 51, 847–855.

Tang, J., Dietzel, M., Böhm, F., Köhler, S.J., Eisenhauer, A., 2008a. Sr^{2+}/Ca^{2+} and $^{44}Ca/^{40}Ca$ fractionation during inorganic calcite formation: II. Ca isotopes. Geochim. Cosmochim. Acta 72, 3733–3745.

Tang, J., Köhler, S.J., Dietzel, M., 2008b. Sr^{2+}/Ca^{2+} and $^{44}Ca/^{40}Ca$ fractionation during inorganic calcite formation: I. Sr incorporation. Geochim. Cosmochim. Acta 72, 3718–3732.

Tang, J., Niedermayr, A., Köhler, S.J., Böhm, F., Kısakürek, B., Eisenhauer, A., Dietzel, M., 2012. Sr^{2+}/Ca^{2+} and $^{44}Ca/^{40}Ca$ fractionation during inorganic calcite formation: III. Impact of salinity/ionic strength. Geochim. Cosmochim. Acta 77, 432–443.

Teng, F.Z., 2017. Magnesium Isotope Geochemistry. In: Teng, F.Z., Watkins, J., Dauphas, N. (Eds.), Non-Traditional Stable Isotopes. Mineralogical Soc Amer & Geochemical Soc, Chantilly, pp. 219–287.

Tesoriero, A.J., Pankow, J.F., 1996. Solid solution partitioning of Sr^{2+}, Ba^{2+}, and Cd^{2+} to calcite. Geochim. Cosmochim. Acta 60, 1053–1063.

Torres-Ruiz, J., 2006. Geochemical Constraints on the Genesis of the Marquesado Iron Ore Deposits, Betic Cordillera, Spain: REE, C, O, and Sr Isotope Data. Econ. Geol. 101, 667–672.

Trail, D., Savage, P.S., Moynier, F., 2019. Experimentally determined Si isotope fractionation between zircon and quartz. Geochim. Cosmochim. Acta 260, 257–274.

Tsipursky, S.J., Buseck, P.R., 1993. Structure of magnesian calcite from sea urchins. Am. Mineral. 78, 775–781.

Urey, H.C., 1947. The thermodynamic properties of isotopic substances. J. Chem. Soc., 562–581

Vaughan, J.R., Hickey, K.A., Barker, S.L.L., 2016. Isotopic, Chemical, and Textural Evidence for Pervasive Calcite Dissolution and Precipitation Accompanying Hydrothermal Fluid Flow in Low-Temperature, Carbonate-Hosted, Gold Systems. Econ. Geol. 111, 1127–1157.

Walter, B.F., Immenhauser, A., Geske, A., Markl, G., 2015. Exploration of hydrothermal carbonate magnesium isotope signatures as tracers for continental fluid aquifers, Schwarzwald mining district, SW Germany. Chem. Geol. 400, 87–105.

Wang, Z., Hu, P., Gaetani, G., Liu, C., Saenger, C., Cohen, A., Hart, S., 2013. Experimental calibration of Mg isotope fractionation between aragonite and seawater. Geochim. Cosmochim. Acta 102, 113–123.

Wang, E.Z., Pang, X.Q., Zhao, X.D., Wang, Z.J., Wang, Z.M., Hu, T., Wu, Z.Y., Yang, J.Q., Feng, Y., Zhang, Z.H., 2020. Characteristics, diagenetic evolution, and controlling factors of the Es1 deep burial high-quality sandstone reservoirs in the PG2 oilfield, Nanpu Sag, Bohai Bay Basin, China. Geol. J. 55, 2403–2419.

Wang, W., Qin, T., Zhou, C., Huang, S., Wu, Z., Huang, F., 2017. Concentration effect on equilibrium fractionation of Mg-Ca isotopes in carbonate minerals: Insights from first-principles calculations. Geochim. Cosmochim. Acta 208, 185–197.

Wang, W., Zhou, C., Liu, Y., Wu, Z., Huang, F., 2019. Equilibrium Mg isotope fractionation among aqueous Mg^{2+}, carbonates, brucite and lizardite: Insights from first-principles molecular dynamics simulations. Geochim. Cosmochim. Acta 250, 117–129.

Wasylenki, L.E., Dove, P.M., Wilson, D.S., De Yoreo, J.J., 2005. Nanoscale effects of strontium on calcite growth: An in situ AFM study in the absence of vital effects. Geochim. Cosmochim. Acta 69, 3017–3027.

Wenk, H.R., Meisheng, H., Lindsey, T., Morris, J.W., 1991. Superstructures in ankerite and calcite. Phys. Chem. Miner. 17, 527–539.

Wombacher, F., Eisenhauer, A., Boehm, F., Gussone, N., Regenberg, M., Dullo, W.C., Rueggeberg, A., 2011. Magnesium stable isotope fractionation in marine biogenic calcite and aragonite. Geochim. Cosmochim. Acta 75, 5797–5818.

Xie, Z., Huang, K.-J., Xia, Y., Cline, J., Tan, Q., Liu, J., Xiao, J., Yan, B., 2022. Heavy $\delta^{26}Mg$ values in carbonate indicate a magmatic-hydrothermal origin of Carlin-type Au deposit. Geochim. Cosmochim. Acta 333, 166–183.

Xiong, D., Azmy, K., Blamey, N.J.F., 2016. Diagenesis and origin of calcite cement in the Flemish Pass Basin sandstone reservoir (Upper Jurassic): Implications for porosity development. Mar. Pet. Geol. 70, 93–118.

Xu, J., Yan, C., Zhang, F., Konishi, H., Xu, H., Teng, H.H., 2013. Testing the cation-hydration effect on the crystallization of Ca-Mg-CO_3 systems. Proc. Nat. Acad. Sci. USA 110, 17750–17755.

Xu, J., Wang, J., Hong, M., Teng, H.H., 2016. Solution-chemistry control of Mg^{2+}-calcite interaction mechanisms: Implication for biomineralization. Am. Mineral. 101, 1104–1112.

Yang, J.H., Zhou, X.H., 2001. Rb-Sr, Sm-Nd, and Pb isotope systematics of pyrite: Implications for the age and genesis of lode gold deposits. Geology 29, 711–714.

Yoshimura, T., Tanimizu, M., Inoue, M., Suzuki, A., Iwasaki, N., Kawahata, H., 2011. Mg isotope fractionation in biogenic carbonates of deep-sea coral, benthic foraminifera, and hermatypic coral. Anal. Bioanal. Chem. 401, 2755.

Young, E.D., Manning, C.E., Schauble, E.A., Shahar, A., Macris, C.A., Lazar, C., Jordan, M., 2015. High-temperature equilibrium isotope fractionation of non-traditional stable isotopes: Experiments, theory, and applications. Chem. Geol. 395, 176–195.

Zhang, S., DePaolo, D.J., 2020. Equilibrium calcite-fluid Sr/Ca partition coefficient from marine sediment and pore fluids. Geochim. Cosmochim. Acta 289, 33–46.

Zhong, S., Mucci, A., 1989. Calcite and aragonite precipitation from seawater solutions of various salinities: Precipitation rates and overgrowth compositions. Chem. Geol. 78, 283–299.

Zhou, J.X., Huang, Z.L., Zhou, M.F., Li, X.B., Jin, Z.G., 2013. Constraints of C-O-S-Pb isotope compositions and Rb-Sr isotopic age on the origin of the Tianqiao carbonate-hosted Pb-Zn deposit, SW China. Ore Geol. Rev. 53, 77–92.

Zhou, G.-T., Zheng, Y.-F., 2002. Kinetic mechanism of oxygen isotope disequilibrium in precipitated witherite and aragonite at low temperatures: an experimental study. Geochim. Cosmochim. Acta 66, 63–71.

Zhu, C., Chen, T., Zhao, L., 2021. Magnesium partitioning into vaterite and its potential role as a precursor phase in foraminiferal Mg/Ca thermometer. Earth Planet. Sci. Lett. 567, 116989.